Solar Phys (2018) 293:151
https://doi.org/10.1007/s11207-018-1370-x

GONG p-Mode Parameters Through Two Solar Cycles

René Kiefer[1,2,3] · Rudi Komm[3] · Frank Hill[3] · Anne-Marie Broomhall[1] · Markus Roth[2]

Received: 18 June 2018 / Accepted: 19 October 2018 / Published online: 9 November 2018

Abstract We investigate the parameters of global solar p-mode oscillations, namely damping width Γ, amplitude A, mean squared velocity $\langle v^2 \rangle$, energy E, and energy supply rate $\mathrm{d}E/\mathrm{d}t$, derived from two solar cycles' worth (1996 – 2018) of *Global Oscillation Network Group* (GONG) time series for harmonic degrees $l = 0 – 150$. We correct for the effect of fill factor, apparent solar radius, and spurious jumps in the mode amplitudes. We find that the amplitude of the activity-related changes of Γ and A depends on both frequency and harmonic degree of the modes, with the largest variations of Γ for modes with 2400 μHz $\leq \nu \leq$ 3300 μHz and $31 \leq l \leq 60$ with a minimum-to-maximum variation of $26.6 \pm 0.3\%$ and of A for modes with 2400 μHz $\leq \nu \leq$ 3300 μHz and $61 \leq l \leq 100$ with a minimum-to-maximum variation of $27.4 \pm 0.4\%$. The level of correlation between the solar radio flux $F_{10.7}$ and mode parameters also depends on mode frequency and harmonic degree. As a function of mode frequency, the mode amplitudes are found to follow an asymmetric Voigt profile with $\nu_{\max} = 3073.59 \pm 0.18$ μHz. From the mode parameters, we calculate physical mode quantities and average them over specific mode frequency ranges. In this way, we find that the mean squared velocities $\langle v^2 \rangle$ and energies E of p modes are anticorrelated with the level of activity, varying by $14.7 \pm 0.3\%$ and $18.4 \pm 0.3\%$, respectively, and that the mode energy supply rates show no significant correlation with activity. With this study we expand previously published results on the temporal variation of solar p-mode parameters. Our results will be helpful to future studies of the excitation and damping of p modes, *i.e.*, the interplay between convection, magnetic field, and resonant acoustic oscillations.

Keywords Helioseismology, observations · Oscillations, solar · Solar Cycle, observations

✉ R. Kiefer
R.Kiefer@warwick.ac.uk

✉ R. Komm
rkomm@nso.edu

1 Centre for Fusion, Space, and Astrophysics, Department of Physics, University of Warwick, Coventry, CV4 7AL, UK

2 Kiepenheuer-Institut für Sonnenphysik, Schöneckstraße 6, 79104, Freiburg, Germany

3 National Solar Observatory, 3665 Discovery Drive, Boulder, CO 80303, USA

1. Introduction

The properties of near-surface convection are subject to slight changes over the course of the activity cycle (*e.g.*, a decrease in granule size in phase with the solar cycle found by Macris *et al.*, 1984; Muller, 1988, and a decrease of granular contrast with increasing level of magnetic activity, see Muller, Hanslmeier, and Saldaña-Muñoz, 2007). As solar p modes are stochastically driven by the acoustic noise generated by convective motion, the related p-mode parameters also vary over the solar activity cycle. However, most previous studies that investigated these activity-related changes of solar p-mode parameters, aside from mode frequencies, were either limited to unresolved solar time series and were thus restricted to low harmonic degrees $l \lesssim 3$ (*e.g.*, Pallé, Régulo, and Roca Cortés, 1990; Elsworth *et al.*, 1993; Chaplin *et al.*, 1998; Howe *et al.*, 2003; Jiménez-Reyes *et al.*, 2004; Salabert *et al.*, 2007; Broomhall, Pugh, and Nakariakov, 2015), or had a very short data baseline to work on (*e.g.*, Jefferies *et al.*, 1991 with 460 hr of data with a 54% duty cycle). Over the last years, little attention has been given to the activity-related changes of solar p-mode parameters for resolved data aside from mode frequencies and frequency splitting coefficients (the exceptions being Komm, Howe, and Hill, 2000b; Korzennik *et al.*, 2013; Korzennik, 2017). Now, with two full solar sunspot cycles' worth of data from the *Global Oscillation Network Group* (GONG) available, we examine the temporal variations of parameters of solar p modes of harmonic degrees $l = 0-150$.

It is well established that mode widths, Γ, which are inversely proportional to the lifetimes of the mode, vary in phase with the level of solar magnetic activity (*e.g.*, Jefferies *et al.*, 1991; Komm, Howe, and Hill, 2000a; Chaplin *et al.*, 2000; Jiménez, Roca Cortés, and Jiménez-Reyes, 2002; Jiménez-Reyes *et al.*, 2003, 2004; Salabert *et al.*, 2007; Burtseva *et al.*, 2009; Broomhall, Pugh, and Nakariakov, 2015). This is taken to indicate that the oscillations are damped by the presence of a magnetic field. The mode amplitudes, A, are observed to be in antiphase with magnetic activity (*e.g.*, Pallé, Régulo, and Roca Cortés, 1990; Elsworth *et al.*, 1993; Chaplin *et al.*, 2000; Komm, Howe, and Hill, 2000a; Jiménez, Roca Cortés, and Jiménez-Reyes, 2002; Jiménez-Reyes *et al.*, 2003, 2004; Broomhall, Pugh, and Nakariakov, 2015). The magnitude of the change of Γ and A depends on both mode frequency and harmonic degree. Along with mode amplitudes, the mean squared velocity $\langle v^2 \rangle$ and energy E of the p modes change with the solar cycle, where highest mode velocities and energies are observed during solar minimum (Komm, Howe, and Hill, 2000b; Jiménez-Reyes *et al.*, 2003; Salabert *et al.*, 2007; Jiménez-Reyes *et al.*, 2004). The energy supply rate to the modes, which is proportional to mode energy times mode width, has been measured not to change throughout the solar cycle for modes of low harmonic degree (Chaplin *et al.*, 2000; Jiménez-Reyes *et al.*, 2003, 2004; Broomhall, Pugh, and Nakariakov, 2015).

In this article, we do not consider mode frequencies. As these are more accessible than the parameters studied here, they have been subject of numerous studies in the past, and their behavior throughout the solar activity cycle is well documented for a wide range of harmonic degrees (*e.g.*, Woodard and Noyes, 1985; Elsworth *et al.*, 1990; Libbrecht and Woodard, 1990; Jiménez-Reyes *et al.*, 1998; Chaplin *et al.*, 2001; Salabert, García, and Turck-Chièze, 2015; Tripathy, Jain, and Hill, 2015; Broomhall, 2017). Mode frequencies are correlated with solar activity, being at their highest during times of strong activity. For very high frequency modes, around and above the acoustic cutoff frequency, this correlation turns into an anticorrelation: the frequencies of these modes are higher during times of weak activity (see, *e.g.*, Woodard and Libbrecht, 1991; Howe *et al.*, 2008; Rhodes *et al.*, 2010). The magnitudes of the shifts of mode frequencies depend on both mode frequency and harmonic degree (see Basu, 2016 and references therein).

This article is structured as follows: The data and the corrections applied to them are described in Section 2. This includes correcting for the spatial masking of GONG Dopplergrams and azimuthal averaging (Section 2.2), and measures to account for the imperfect duty cycle (Section 2.3) and for spurious jumps in the mode parameters (Section 2.4). We present our results for the temporal variation of mode widths and amplitudes in Section 3 and focus on the temporal average of the mode amplitudes in Section 3.3. We proceed to consider the temporal variation of the quantities mean squared velocity, energy, and energy supply rate of the p modes (Section 4). A summary and discussion of our findings is given in Section 5.

2. Data and Method

2.1. Data Sets

In the present analysis, we use mode parameter data that were produced by the standard GONG pipeline (Anderson *et al.*, 1990; Hill *et al.*, 1996; Hill and Howe, 1998) from solar full-disk Dopplergrams.[1] The mode parameters were obtained by fitting symmetric Lorentzian profiles to the power spectra of 108-day-long datasets, where every third dataset was independent, *i.e.*, they overlapped by 72 days. These time series were concatenations of three GONG months, with one GONG month being 36 days. This ensures a reasonable frequency resolution of the fitted power spectra and number of independent data points. The power spectra were computed and fit for all harmonic degrees l and azimuthal orders $-l \leq m \leq l$ up to $l = 150$. The model that was fit to each peak in the power spectra consisted of a linear two-parameter background and a Lorentzian profile, which depends on the parameter width Γ, amplitude A, and frequency ν. Mode frequencies and the background parameters are not considered in the following. The GONG peak-fitting algorithm fits symmetric Lorentzian profiles to the spectra (Hill *et al.*, 1996). Since the mode peaks are known to be asymmetric (*e.g.*, Nigam *et al.*, 1998), this might introduce small, temporally varying systematics to the mode parameter analyzed, as the asymmetry changes over the solar cycle (Jiménez-Reyes *et al.*, 2007; Korzennik, 2013; Howe *et al.*, 2015).

2.2. Azimuthal Averaging and Correction for Spatial Masking

In full-disk images of the Sun, pixels close to the solar limb are subject to several unwanted effects. First, because GONG measures line-of-sight velocities, projection effects increase toward the solar limb. Second, the resolution of each pixel, measured in distance on the solar surface, increases toward the limb. A spatial mask is applied in the GONG pipeline to cut away these unwanted pixels. This leads to a suppression of mode amplitudes depending on the ratio of azimuthal order and harmonic degree $|m/l|$: While spherical harmonics with $m = 0$ oscillate over all latitudes (with a temporal dependence of $\mathrm{e}^{-\mathrm{i}\omega t}$, where ω is the angular frequency), spherical harmonics with azimuthal order $m \neq 0$ are confined to latitudes closer to the equator. The confinement to low latitudes becomes more pronounced for higher harmonic degree and higher $|m/l|$. Therefore, by masking out regions near the solar limb, more mode power is cut away from modes with low $|m/l|$ than from those with higher $|m/l|$. In contrast, the damping width of a mode in a power spectrum, representing the lifetime of the mode, is negligibly affected by the masking.

[1]The data are publicly available online and can be downloaded here: ftp://gong2.nso.edu/TSERIES/.

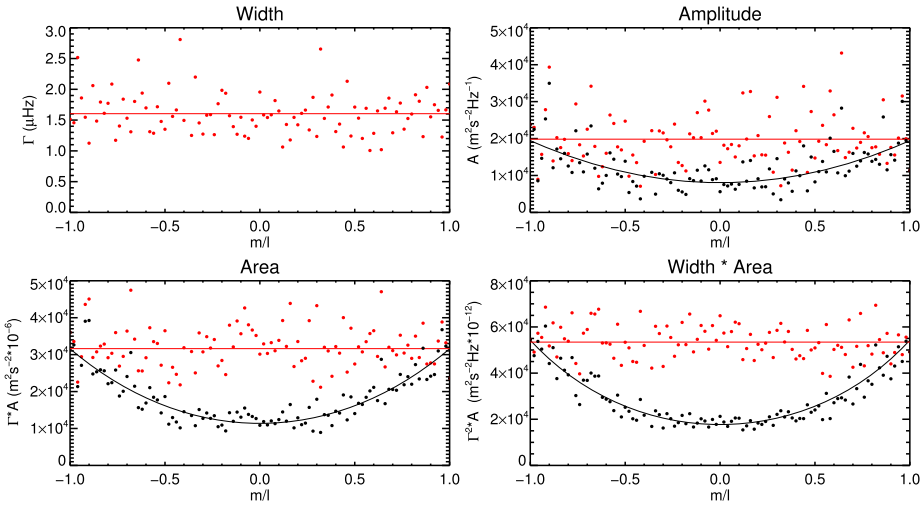

Figure 1 Correction for the effects of the spatial masking for the mode $(n, l) = (10, 50)$ in GONG month 5. *Black data points* are measurement values. *Solid black lines* are polynomial fits to the data to account for the effect of the spatial masking. *Red data points* are the corrected values. *Solid red lines* indicate the weighted mean of the corrected data.

Figure 1 shows the outputs of the GONG pipeline for mode width Γ, amplitude A, and the products $\Gamma \cdot A$ and $\Gamma^2 \cdot A$ of the mode $(n, l) = (10, 50)$ from GONG month 5, where n is the radial order. In the top left panel, the mode widths of the azimuthal components are shown as a function of m/l, but no visible dependence is observed. The solid red line is the error-weighted mean of the data. In the top right panel, the black data points are the measured values of the mode amplitudes. As discussed above, mode amplitudes and products that include mode amplitudes show a dependence on m/l, which is introduced by the spatial mask. It is accounted for by fitting a polynomial proportional to $(m/l)^{2k}$ with $k = 0, 1, 2$ to the data. This polynomial function is empirically determined (see Komm, Howe, and Hill, 2000a). The resulting fit is shown as a solid black line in the top right and two lower panels of Figure 1. The dependence is then removed, where the values at $|m/l| = 1$ are kept constant. The error-weighted mean of the corrected data points is adopted as the representative value of the mode parameter (shown as a solid red line). In order to obtain meaningful weighted mean values, in the subsequent analysis, only those multiplets are included for which at least one-third of the azimuthal components are fit by the GONG pipeline. This minimum number of fit components is set to two-thirds for modes with low harmonic degree $l \leq 10$, to account for their small number of azimuthal components. In the following, we avoid the term *multiplet*, as only azimuthal averages are considered, and we use the term *mode* instead.

2.3. Correction for Window Function

The temporal fill factor of GONG is lower than unity. This leads to a redistribution of the power from the mode peak to neighboring frequency bins and into side lobes of the main peak, which in turn results in a diminished mode amplitude and an increased mode width. The side lobes are caused by repeating gaps in the data. These side lobes, especially those caused by daily gaps, are considerably suppressed for a network distributed around the globe

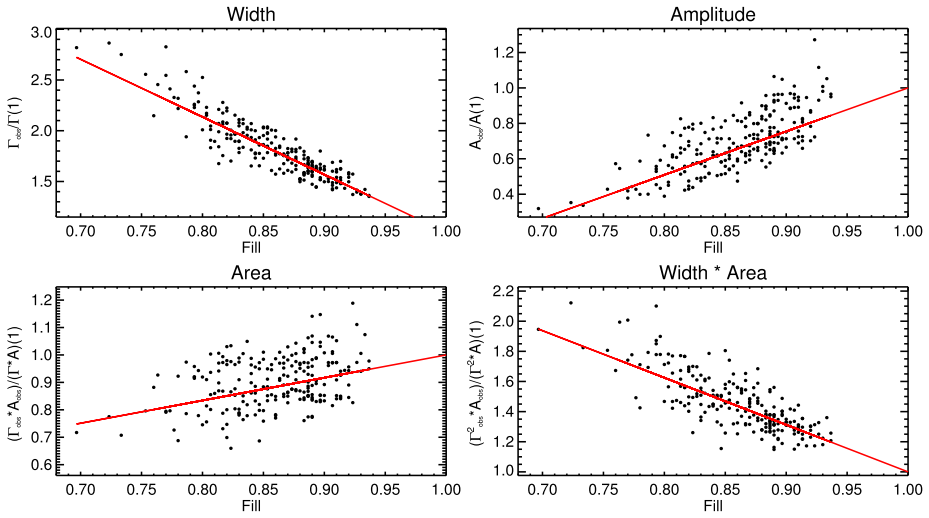

Figure 2 Correction of the effect of the temporal window function on mode parameters of mode $(n, l) = (10, 50)$. Parameter values are shown as a function of the temporal fill factor of the individual GONG months. Linear fits to the data are shown as *red lines*. Data are normalized to the value of the linear fit at fill $= 1$.

as GONG is (Hill *et al.*, 1996; Leibacher, 1999). A machine-readable table with the fill factor of each 36-day GONG month is available at https://gong2.nso.edu/fill.txt. The specific structure of the gaps does not have to be taken into account as the fill factor is rather high, with values between 69% and 93%. To account for the impact of gaps, we adopted the approach described in Komm, Howe, and Hill (2000b), who showed that a linear regression is sufficient to correct for the effect of the temporal window function of GONG data.

In Figure 2, the mode width Γ, mode amplitude A, mode area $\Gamma \cdot A$, and mode width times mode area $\Gamma^2 \cdot A$ of the mode $(n, l) = (10, 50)$ are shown as a function of fill factor. The products $\Gamma \cdot A$ and $\Gamma^2 \cdot A$ are used in Section 4 to calculate the quantities of mean squared velocity, mode energy, and energy supply rate of the modes. The data are normalized to the value of the linear regression at fill $= 1$. To obtain the corrected parameter values, the resulting fit of a linear function, shown as a red line in each panel of Figure 2, is first subtracted from the data and then its value at fill $= 1$ is added. As previously demonstrated by, *e.g.*, Komm, Howe, and Hill (2000a), mode widths increase with decreasing fill factor and amplitudes decrease with decreasing fill factor. It should be noted that the background amplitude increases with decreasing fill factor. This indicates that power from the mode peaks is indeed distributed into the background.

2.4. Correction for Jumps in Sensitivity

There are two jumps in the mode amplitudes that we corrected for with an empirical correction factor. The first jump around GONG month 60 is due to a camera upgrade. The second jump around month 100 is of uncertain origin. The correction factor C is given in Equation 12 in Appendix A. More details about the applied corrections and the jumps are given in Appendix A.

2.5. Proxy for Solar Activity

Many quantities connected to the Sun are known to vary with the solar activity cycle, *e.g.*, the sunspot number and the emission in the Ca II H & K lines. Here, we use the solar radio flux $F_{10.7}$ as a proxy for the level of solar activity.[2] The $F_{10.7}$ is the total emission on the solar disk at a wavelength of 10.7 cm integrated over one hour. $F_{10.7}$ is measured in *solar flux units* sfu, where 1 sfu $= 10^{-22}$ W m^{-2} Hz^{-1}. The $F_{10.7}$ index is the averaged $F_{10.7}$ flux scaled for 1 AU. It is a proxy for the level of activity in the upper chromosphere and the lower corona (Tapping, 2013). A comparison of different proxies of solar magnetic activity and their correlation with the activity-related frequency shifts of solar p modes over the last three solar cycles can be found in Broomhall and Nakariakov (2015).

3. Temporal Variation of Mode Parameters

3.1. Mode Widths

To obtain clear results on their temporal variation, mode parameters have to be averaged over many modes. From here on, only modes that are present at all time samples are considered. The analysis of both mode widths and mode amplitudes is restricted to modes with frequencies 1500 μHz $\leq \nu \leq$ 4500 μHz and harmonic degree $0 \leq l \leq 150$. This results in a set of 1275 mode widths and 1272 mode amplitudes. Different error flags for bad mode widths and amplitudes result in the small difference in the number of modes in the sets. As both mode widths and amplitudes are dependent on mode frequency and harmonic degree, they are normalized to the mean over all time samples for each mode individually. Next, the normalized parameters of all included modes are averaged. The result for the observed mode widths $\Gamma_{\text{obs, mean}}$ is shown in the first panel of the top row of Figure 3. Here, the correction for the effect of the fill factor has not yet been applied. The need for such a correction can be seen from the middle panel of the top row, where the same data are plotted as a function of fill factor. The linear dependence on fill is apparent. In the right panel, the mode widths are shown as a function of the $F_{10.7}$ index. The red data points in all panels of Figure 3 indicate time samples with higher than median level of activity as computed from the $F_{10.7}$ flux.

In the middle row of Figure 3, the mode widths $\Gamma_{\text{fill=1,mean}}$ are shown after the correction for the temporal window function. A second correction is required to account for the apparent change in solar radius throughout the year. This change affects the measured values of oscillation parameters as the spatial resolution of the Dopplergrams changes with it. We applied a linear correction to the mode parameters as a function of apparent solar radius to correct for this. The bottom row shows the mode widths $\Gamma_{\text{fill=1,radius,mean}}$ after both the effect of the fill factor and the change of the apparent solar radius have been removed.

For better visibility, the left panel of the bottom row of Figure 3 is shown again in the top panel of Figure 5. As can be seen, the uncertainties on the normalized variation of the mode widths are on the order of a few tenths of a percent. The error bars given here are computed as the standard error of the mean. The solid black line is the one-year running average. The red line is the $F_{10.7}$ index. It is boxcar smoothed over one year and scaled to match the extrema of the one-year boxcar-smoothed variation of the mode widths. The correlation coefficient (Spearman's rank correlation coefficient ρ) between the variation of the width

[2]The $F_{10.7}$ time series that was used in this work can be downloaded from this website: spaceweather.gc.ca/solarflux/sx-5-en.php.

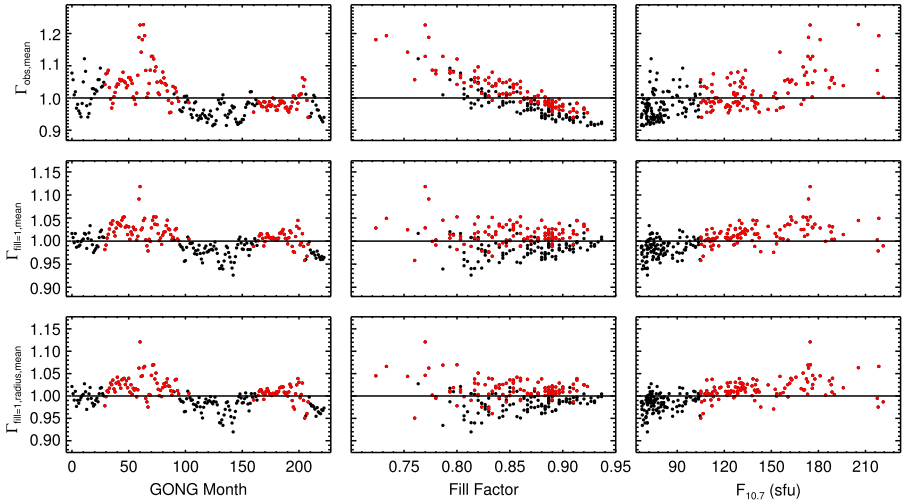

Figure 3 Normalized mode widths averaged over all modes as a function of time (*left column*), fill factor (*middle column*), and of the magnetic activity proxy $F_{10.7}$ index (*right column*). The *top row* shows the raw data, the *middle row* is normalized for the effects of the fill factor, and the *bottom row* is corrected for fill and for change in apparent radius of the Sun.

and the $F_{10.7}$ index (both unsmoothed) is $\rho = 0.62$ with $p = 2 \cdot 10^{-9}$. Only independent data points were used to calculate this. The number of independent data points is 74, *i.e.*, every third GONG 108-day dataset. We used Spearman's ρ to asses the level of correlation of the two quantities as the relation between mode widths and activity is not strictly linear: As can be seen from the right panel in the bottom row in Figure 3, the variation of mode widths increases with the level of the $F_{10.7}$ index. However, for values of $F_{10.7} \gtrsim 130$, mode widths appear to be in saturation. The largest discrepancy between the $F_{10.7}$ index and the mode widths can be seen during the time of the camera upgrade in the GONG network around month 60 (in 2001). Averaged over all modes, the minimum-to-maximum variation of the one-year boxcar-smoothed variation of mode widths is $11.5 \pm 0.2\%$.

In Figure 6, the normalized variation of averages of mode widths (after the corrections for fill and apparent solar radius variation have been applied) for modes of different frequency and harmonic degree ranges are shown as a function of time. Table 3 in Appendix B holds information on the number of modes used in each panel of Figure 6, the minima and maxima of the parameter variation, the mean uncertainty of each data point, and the correlation of mode widths with the $F_{10.7}$ index.

The minimum-to-maximum variation of the mode widths over the two observed solar cycles is dependent on mode frequency and harmonic degree. The largest fractional variation is found for modes with 2400 μHz $\leq \nu \leq$ 3300 μHz and $31 \leq l \leq 60$ with a minimum-to-maximum variation of $26.6 \pm 0.3\%$. The smallest variation of mode widths is found for the modes in the 1500 μHz $\leq \nu \leq$ 2400 μHz and $101 \leq l \leq 150$ parameter regime with a minimum-to-maximum variation of $5.5 \pm 0.2\%$. To suppress the impact of outliers on these minimum-to-maximum variations, they were calculated for the one-year boxcar-smoothed values of the mode widths. The middle frequency range with 2400 μHz $\leq \nu \leq$ 3300 μHz shows the largest minimum-to-maximum variation over the solar cycle for each subset of modes of the same range of harmonic degrees. The exception to this is the subset of modes

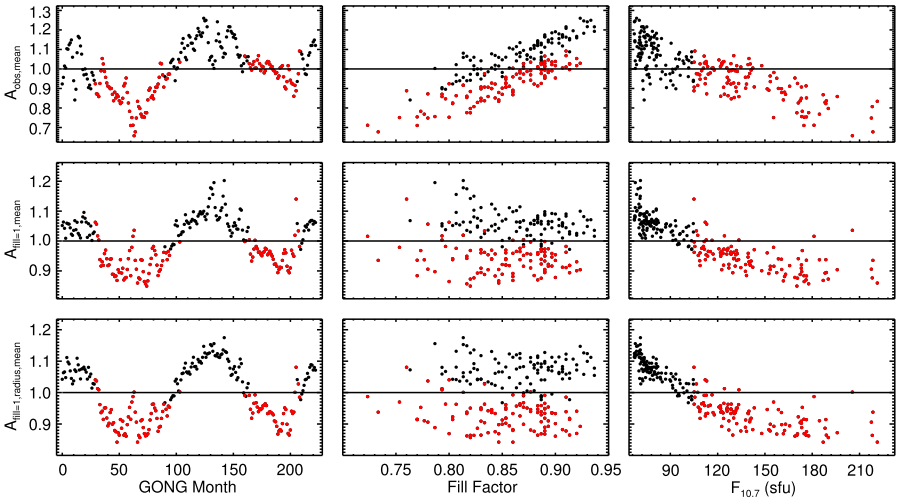

Figure 4 Same as Figure 3, but for mode amplitudes.

with $101 \leq l \leq 150$, for which the variation over the solar cycle is largest for modes in the high-frequency range.

The last two columns of Table 3 give the correlation between the variation of mode widths and the $F_{10.7}$ index as well as the associated two-sided significance value. The highest level of correlation is found for modes with 1500 μHz $\leq \nu \leq$ 2400 μHz and $0 \leq l \leq 30$, with a Spearman's rank correlation coefficient of $\rho = 0.84$ and a two-sided significance of $p < 10^{-10}$. The lowest correlation is found for modes with 1500 μHz $\leq \nu \leq$ 2400 μHz and $31 \leq l \leq 60$, with $\rho = 0.31$ and $p \approx 0.01$. Within each range of harmonic degrees, the correlation coefficient increases with mode frequency. The exception to this are modes with $0 \leq l \leq 30$, where modes in the middle frequency range show the highest level of correlation with the $F_{10.7}$ index.

3.2. Mode Amplitudes

In Figure 4 the mode amplitudes A are shown as functions of time, fill, and $F_{10.7}$ index (columns) and for three levels of correction (rows), as was previously described for the mode widths (Figure 3). The effect of the correction for the change in apparent size of the Sun is more pronounced for mode amplitudes than it is for mode widths. As can be seen in the left panel of the middle row, there is a distinct yearly variation in the mode amplitudes $A_{\text{fill=1,mean}}$ after the fill correction has been applied. This is largely removed in the left panel of the bottom row. The change to the mode amplitudes due to this correction is most obvious through months 110 – 150, which corresponds to the activity minimum between Cycles 23 and 24. In the right panel of the bottom row of Figure 4, mode amplitudes $A_{\text{fill=1,radius,mean}}$ are shown as a function of the $F_{10.7}$ index. A clear anticorrelation between the two quantities is visible. For levels of activity up to $F_{10.7} \approx 130$, the relation appears linear. For higher levels of activity, there is little to no change in mode amplitudes, similar to the behavior seen for mode widths (Figure 3).

The normalized, averaged, and corrected temporal variation for mode amplitudes is shown in the lower panel of Figure 5. The last row of Table 4 in Appendix B gives more detailed information about the number of modes within each parameter range and the error

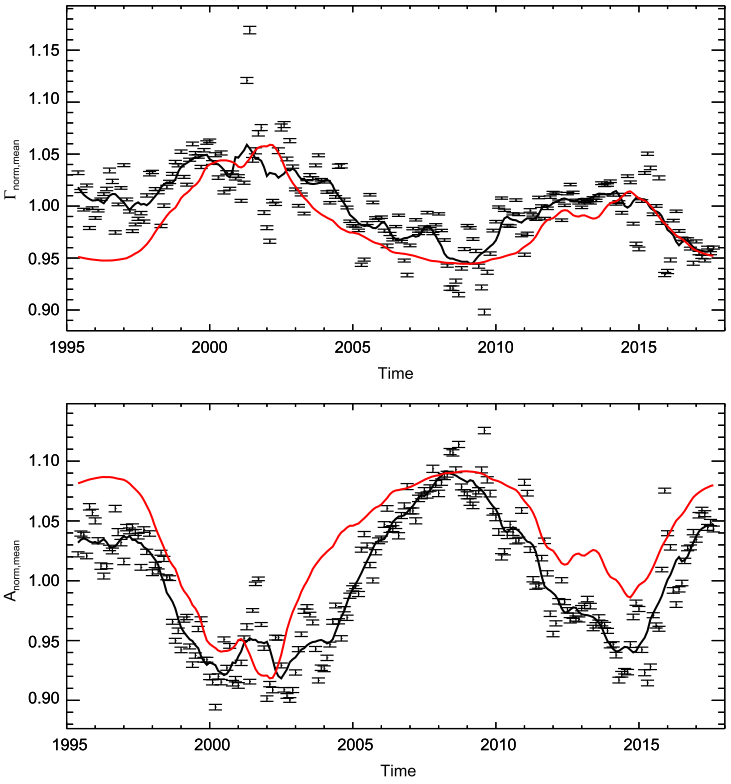

Figure 5 *Top panel:* Normalized mode widths averaged over all modes (*black data points*). *Error bars* indicate the error of the mean. The *solid black line* is the one-year average of the mode widths. The *red line* is the $F_{10.7}$ solar radio flux as a function of time smoothed by boxcar with a width of one year. It is scaled to match the variation of the mode widths. *Bottom panel:* Same as *top panel*, but for mode amplitudes. The $F_{10.7}$ radio flux was flipped for better appreciation of the anticorrelation of the change in mode amplitudes and the level of activity.

bars presented in this plot. The error bars in Figure 5 were computed as the standard error of the mean. The solid lines are the data (black) and $F_{10.7}$ index (red) smoothed with a one-year boxcar. The $F_{10.7}$ index is scaled to match the minimum-to-maximum variation of the mode amplitudes and flipped for better appreciation of the anticorrelation of the two quantities. Averaged over all modes, the minimum-to-maximum variation is $17.3 \pm 0.2\%$. The correlation coefficient (Spearman's rank correlation coefficient) between amplitudes and the $F_{10.7}$ index (both unsmoothed) is $\rho = -0.91$ with $p < 10^{-10}$. Only independent data points were used in the computation of the correlation coefficient.

The equivalent of Figure 6, where the normalized variation of mode widths is shown for different mode parameter regimes, is presented in Figure 7 for mode amplitudes. Detailed information on the individual panels is given in Table 4 in Appendix B. The largest variation is found for modes with $2400\ \mu\text{Hz} \leq \nu \leq 3300\ \mu\text{Hz}$ and $61 \leq l \leq 100$ with a minimum-to-maximum variation of $27.4 \pm 0.4\%$. Modes with frequencies $1500\ \mu\text{Hz} \leq \nu \leq 2400\ \mu\text{Hz}$ and harmonic degrees $0 \leq l \leq 30$ exhibit the smallest variation over the 22 years of data, with a fractional change of $11.6 \pm 0.5\%$. The anticorrelation between the level of activity and the change in mode amplitudes is highest for modes with $2400\ \mu\text{Hz} \leq \nu \leq 3300\ \mu\text{Hz}$

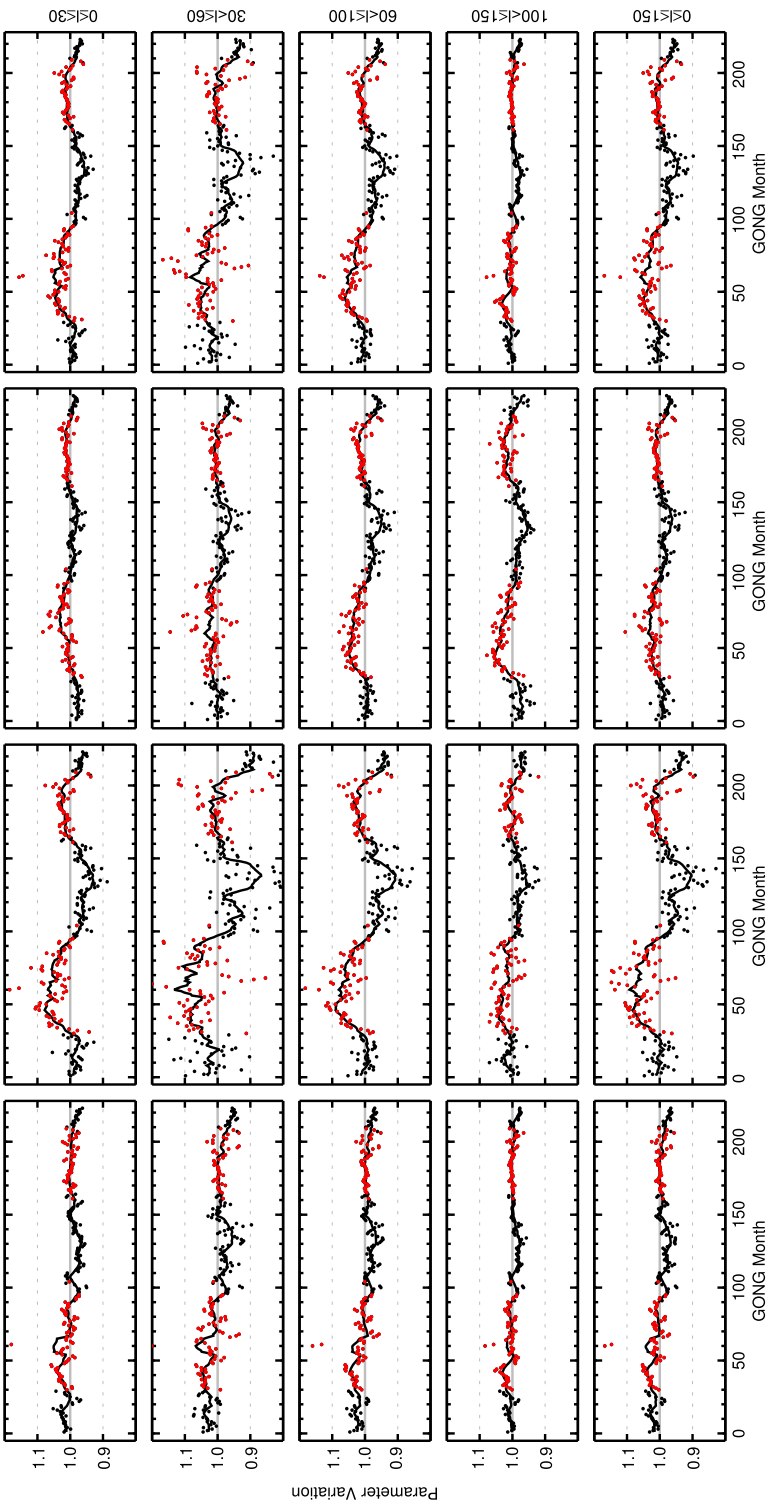

Figure 6 Temporal variation of mode widths for different ranges of harmonic degrees (*rows*, harmonic degree range indicated to the right of the fourth column) and mode frequencies (*columns*, frequency range indicated above the first row). Widths are normalized to the mean for each mode and then averaged over all modes in the respective range of frequency and degree. Months with higher than median $F_{10.7}$ solar radio flux are highlighted by *red points*. The one-year average is shown by the *solid black line*. Levels of 1.1 and 0.9 of the mean are indicated by *gray dashed lines*.

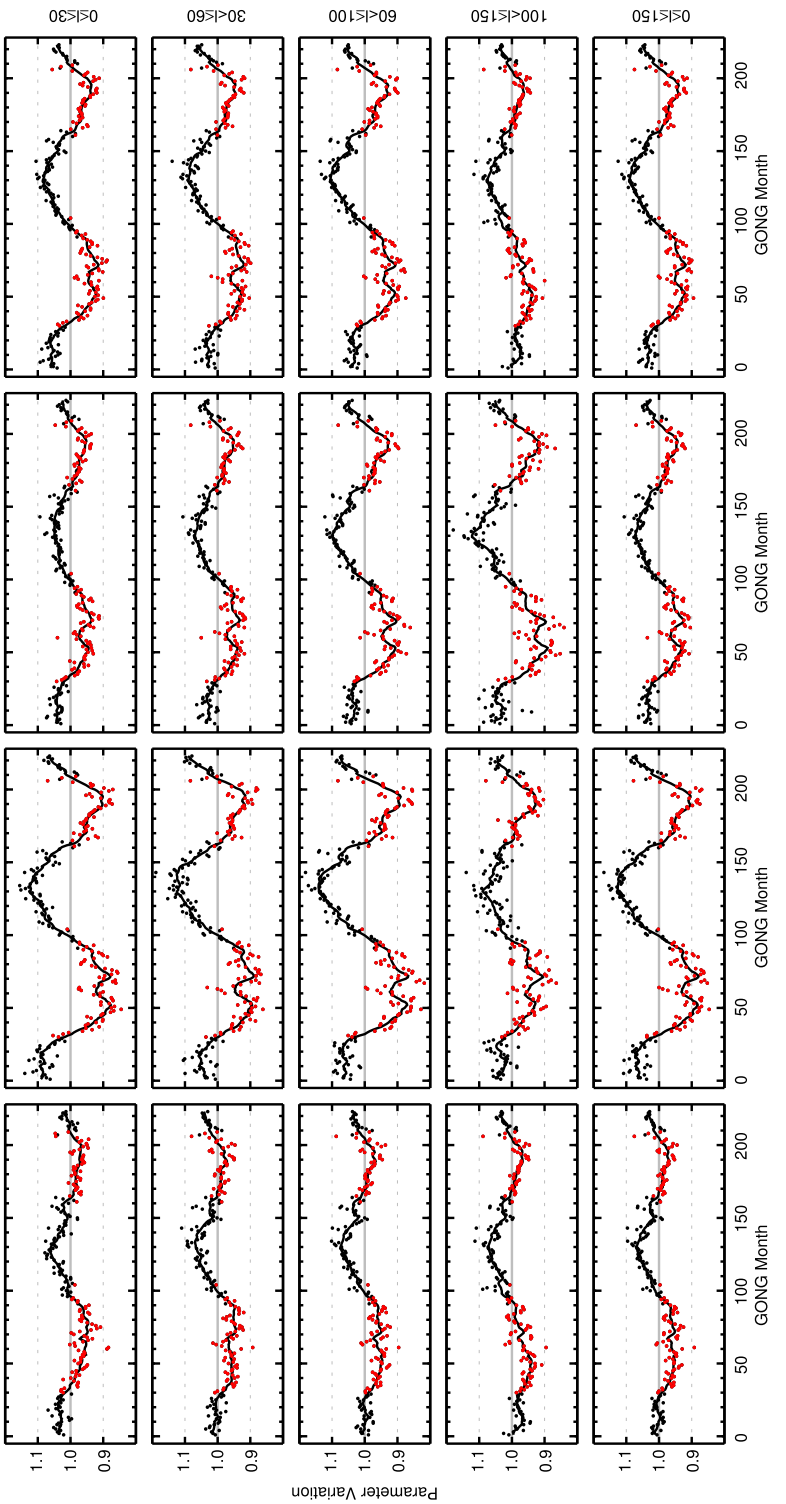

Figure 7 Same as Figure 6, but for mode amplitudes.

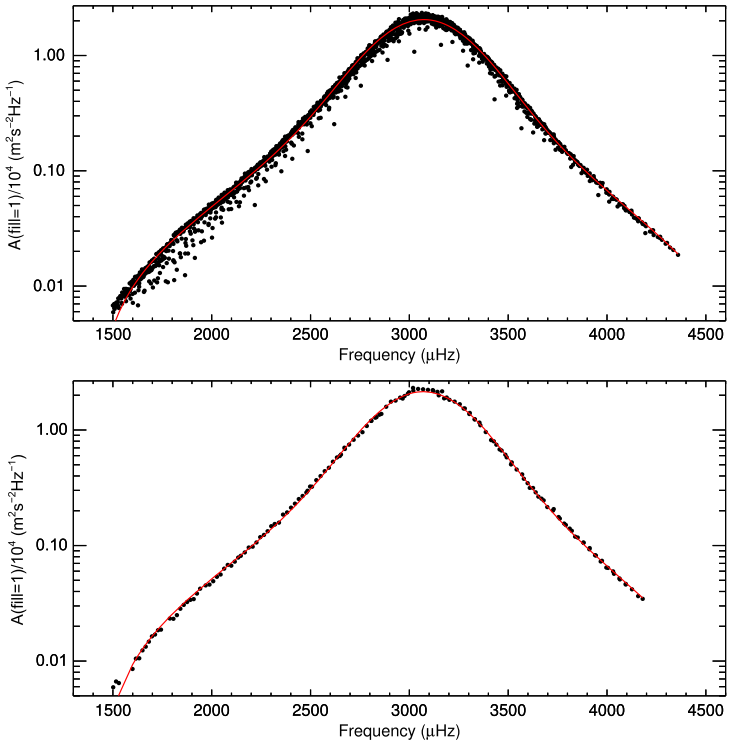

Figure 8 Mode amplitudes as a function of mode frequency. Amplitudes are averaged over all GONG months after correction for the fill factor. The *red curve* is an asymmetric Voigt profile fit to the data. *Top panel*: Amplitudes of modes with $2 \leq l \leq 150$. *Bottom panel:* Amplitudes of modes with $31 \leq l \leq 40$.

and $0 \leq l \leq 30$ with a rank correlation of $\rho = -0.94$ and $p < 10^{-10}$. For the three ranges of harmonic degrees (l between 0 – 30, 31 – 60, and 61 – 100) the largest variation is found in the middle frequency range (2400 – 3300 μHz). For modes with $101 \leq l \leq 150$, this is observed for the high-frequency modes.

3.3. Frequency Distribution of Mode Amplitudes

In the top panel of Figure 8, the amplitudes of all modes with $2 \leq l \leq 150$, which are present in at least 50% of the GONG months, are shown as a function of mode frequency on a logarithmic ordinate divided by 10^4. Here, the amplitudes interpolated to fill = 1 were used. Any variation due to the residual change in apparent solar radius was averaged out as the data cover 22 years. By lowering the presence rate to 50%, more modes, especially of $l \gtrsim 100$, were included and the mode amplitudes could be investigated for separate ranges of harmonic degrees (see the bottom panel of Figure 8 for an example). This increased the total number of included modes from 1272 to 1543.

The solid red lines in Figure 8 are fits of asymmetric Voigt profiles to the mode amplitudes. This profile is described by

$$V(\nu) = \mathcal{A} \cdot \left(b + a \cdot \int_{-\infty}^{\infty} G(x) L(\nu - x)\, \mathrm{d}x \right), \tag{1}$$

where b is an offset, a is a factor to adjust the height of the profile, and the integral extends over the entire frequency axis with frequencies x. The Gaussian function $G(\nu)$ and the Lorentz function $L(\nu)$ in Equation 1 are given by

$$G(\nu) = \frac{\exp(-\nu/2\sigma^2)}{\sigma\sqrt{2\pi}}, \tag{2}$$

$$L(\nu) = \frac{\gamma}{\pi(\nu^2+\gamma^2)}, \tag{3}$$

with the standard deviation of the Gaussian σ and the half-width at half-maximum of the Lorentzian γ. The asymmetry is introduced with the function

$$\mathcal{A} = \frac{1}{\pi}\left(\tan^{-1}\left(S\cdot(\nu-\nu_{\max})/\Sigma\right)+0.5\right), \tag{4}$$

where S is the asymmetry parameter, $\nu_{\max}$ is the frequency of the maximum of the symmetric Voigt profile, and the full width at half-maximum of the Voigt profile, Σ, can be approximated by (Whiting, 1968; Olivero and Longbothum, 1977)

$$\Sigma = 1.0692\gamma + \sqrt{0.86639\gamma^2 + 8\ln(2)\sigma^2}. \tag{5}$$

The resulting fit parameters for amplitudes of modes with $2 \le l \le 150$ are given in Table 1. For the frequency of maximum amplitude, we find $\nu_{\max} = 3079.76 \pm 0.17$ μHz. The width of the Voigt profile is $\Sigma = 611.8 \pm 0.5$ μHz. The parameter $S = -0.100 \pm 0.002$ indicates that the distribution is slightly left-tailed (left-skewed, right-leaning). The χ^2_{red} of the fit is 32.8. This rather high χ^2_{red} value is due to the spread in the distribution of the mode amplitudes for modes of different harmonic degree and the small error bars. Other profiles were tested (pure Gaussian, pure Lorentzian, both Gaussian and Lorentzian including asymmetry), but the asymmetric Voigt yielded the best χ^2_{red}. We excluded modes with $l = 0, 1$ because their amplitudes are less well defined, and including them here would increase the χ^2_{red} to ≈ 135.

It should be noted that the maximum of the mode amplitudes $\nu_{\max}$ presented here is not exactly what is often referred to as $\nu_{\max}$ in the literature. It is usually measured from Sun-as-a-star data, which only include low harmonic degrees up to $l \lesssim 4$ (Broomhall *et al.*, 2009). Here, $\nu_{\max}$ is the maximum of the mode amplitudes in the frequency spectrum of the spherical harmonic transform of the GONG Doppler velocity data for all harmonic degrees up to $l = 150$. Typical values for $\nu_{\max}$ include 3050 μHz by Kjeldsen and Bedding (1995), 3104 μHz as a calibrated value to obtain better results from asteroseismic scaling relations by Mosser *et al.* (2013), and 3120 μHz from SOHO/VIRGO data by Kallinger *et al.* (2010). If $\nu_{\max}$ is measured from the velocity of the modes (as we discuss in Section 4, the mean velocity of the modes is proportional to mode width Γ times mode amplitude A), the damping widths Γ are included in the measured quantity. As mode widths change with mode frequency and harmonic degree (see next section), the maxima in mode amplitude A and mean velocity of the modes (proportional to $\Gamma \cdot A$) occur for slightly different frequencies.

We also investigated the mode amplitudes for smaller ranges of harmonic degrees. For this, we separated the modes into groups of typically ten harmonic degrees. As an example, we show the amplitudes of modes with $31 \le l \le 40$ (black data points) and the fit of an asymmetric Voigt profile (solid red line) in the lower panel of Figure 8. As can be seen from Figure 8, the frequency dependence of the amplitudes of modes of similar harmonic degree is well captured by the asymmetric Voigt profile. The resulting fit parameters for this and

Table 1 Fit parameters of the frequency distribution of mode amplitudes for modes with $2 \leq l \leq 150$.

$\nu_{\max}$ [μHz]	σ [μHz]	γ [μHz]	Σ [μHz]
3079.76 ± 0.17	181.8 ± 0.3	150.9 ± 0.2	611.8 ± 0.5
$a/10^4$ [$\mathrm{m^2\,s^{-2}\,Hz^{-1}}$]	b [$\mathrm{m^2\,s^{-2}\,Hz^{-1}}$]	S	χ^2_{red}
3299 ± 2	-581 ± 1	-0.100 ± 0.002	32.8

more ranges of harmonic degrees are presented in Table 5 in Appendix C. There, we also show figures of the change of the fit parameters with harmonic degree. Except for the width of the Voigt profile Σ, all parameters show systematic variations with mode degree. The frequency of maximum amplitude $\nu_{\max}$ has a maximum value for intermediate-degree modes and decreases substantially at low and high degrees (below $l = 30$ and above $l = 90$). The skewness S is anticorrelated with $\nu_{\max}$. The width Σ is approximately constant, except for the band of highest harmonic degrees considered. Amplitudes first increase with harmonic degree, reach a maximum around $l \approx 40$, and then decrease again.

4. Results for Physical Quantities

The amplitude A is given as power per frequency bin $\mathrm{m^2\,s^{-2}\,Hz^{-1}}$. Hence, calculating the product of mode width and mode amplitude $\Gamma_{nl} \cdot A_{nl}$ has the unit of squared velocity. The mean squared velocity of the modes can be calculated as (Goldreich, Murray, and Kumar, 1994)

$$\left\langle v_{nl}^2 \right\rangle = \frac{\pi}{2} C_{\mathrm{vis}} \Gamma_{nl} A_{nl}. \tag{6}$$

Symmetric Lorentzian profiles are fitted to the peaks in the power spectrum by the GONG pipeline. This is taken into account by the scaling factor $\pi/2$. The quantity $\Gamma_{nl} \cdot A_{nl}$ is referred to as the *mode area*, *i.e.*, the area below the fitted peak in the spectrum (Komm, Howe, and Hill, 2000b). The factor $C_{\mathrm{vis}} = 3.33$ corrects for the reduced visibility of modes due to leakage effects (Hill and Howe, 1998).

Because of the different cavities in which modes of different harmonic degree and frequency propagate, the fraction of the mass of the Sun that is affected by different modes varies (see, *e.g.*, Basu, 2016). The *mode mass* M_{nl} is given by

$$M_{nl} = M_\odot I_{nl}, \tag{7}$$

where $M_\odot$ is the solar mass and the mode inertia is calculated as (Christensen-Dalsgaard and Berthomieu, 1991)

$$I_{nl} = \frac{4\pi \int_0^{R_\odot} \rho(r) (\xi_{nl}^r(r)^2 + l(l+1)\xi_{nl}^h(r)^2) r^2 \,\mathrm{d}r}{M_\odot (\xi_{nl}^r(R_\odot)^2 + l(l+1)\xi_{nl}^h(R_\odot)^2)}. \tag{8}$$

Here, ξ_{nl}^r and ξ_{nl}^h are the radial and horizontal displacement eigenfunctions associated with the oscillation, $\xi_{nl}^r(R_\odot)$ and $\xi_{nl}^h(R_\odot)$ are their values at the photospheric radius, and ρ is the mass density. We calculated mode inertias from the eigenmodes of the standard solar model 'Model S' (Christensen-Dalsgaard *et al.*, 1996).

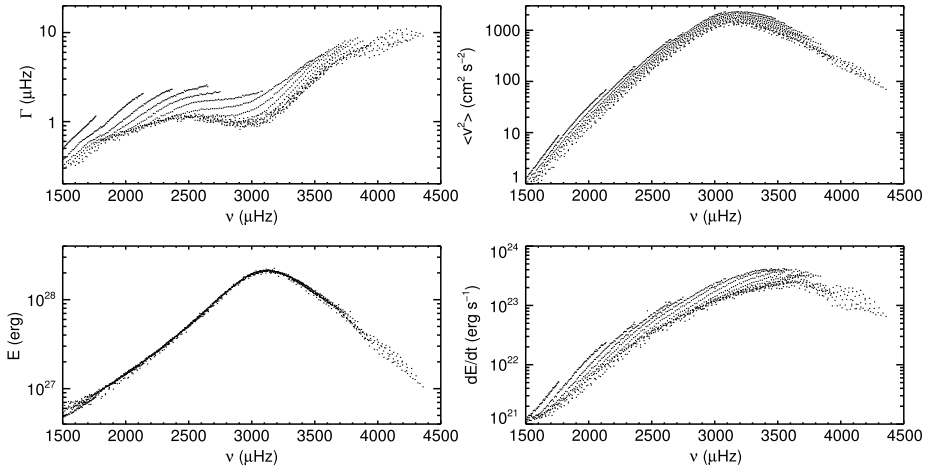

Figure 9 Mode widths Γ, mean squared velocity $\langle v^2 \rangle$, mode energies E, and energy supply rates $\mathrm{d}E/\mathrm{d}t$ as functions of frequency. All quantities are averaged over all GONG months.

The energy that is stored in the modes can be calculated as the product of mode mass (Equation 7) and mean squared velocity (Equation 6):

$$E_{nl} = M_{nl} \langle v_{nl}^2 \rangle. \tag{9}$$

This is the total mode energy, *i.e.*, the sum of kinetic and potential energy (Goldreich, Murray, and Kumar, 1994). The rate at which energy is supplied to the modes can be calculated by the product of the energy in the modes and the radian damping rate of the modes $2\pi\,\Gamma_{nl}$ (Kumar, Franklin, and Goldreich, 1988; Goldreich, Murray, and Kumar, 1994):

$$\frac{\mathrm{d}E_{nl}}{\mathrm{d}t} = 2\pi\, E_{nl} \Gamma_{nl} = \pi^2 C_{\mathrm{vis}} M_{nl} A_{nl} \Gamma_{nl}^2, \tag{10}$$

which is proportional to the product of squared mode width Γ_{nl}^2 and mode amplitude A_{nl}.

In Figure 9 the mode width (damping rate) Γ, mean squared velocity $\langle v_{nl}^2 \rangle$, mode energy E, and energy supply rate $\mathrm{d}E/\mathrm{d}t$ of modes with harmonic degree $l > 10$ are shown on logarithmic scales as functions of mode frequency. Modes with $l \leq 10$ are excluded here to further reduce the scatter in these plots. The parameters of these modes are less well defined owing to their small number of azimuthal components, see Section 2.2. For each mode, the values for Γ, A, $\Gamma \cdot A$, and $\Gamma^2 \cdot A$ were calculated as the mean over all time samples after correction for the fill factor. Any effects from the activity cycle or residual yearly variations were averaged out as the dataset spans two complete Schwabe cycles. The conversion of these quantities into physical units was then made according to Equations 6, 9, and 10.

The mode widths (upper left panel in Figure 9) increase from 0.3 – 0.5 μHz at low mode frequencies $\approx$1500 μHz to values between 1 – 2 μHz for mode frequencies between 2400 – 3000 μHz. For higher mode frequencies, mode widths increase again, reaching $\Gamma \approx 10$ μHz for the highest mode frequencies. The mean squared velocity (upper right panel) increases monotonically with mode frequency until it reaches its maximum for modes with frequencies of $\approx$3200 μHz. The maximum mean velocity value is $v \approx 37\ \mathrm{cm\,s^{-1}}$. The mode widths, mean squared velocity, and the energy supply rate (lower right panel) show ridges of modes with equal radial order. Different ridges are slightly offset from one another, but show

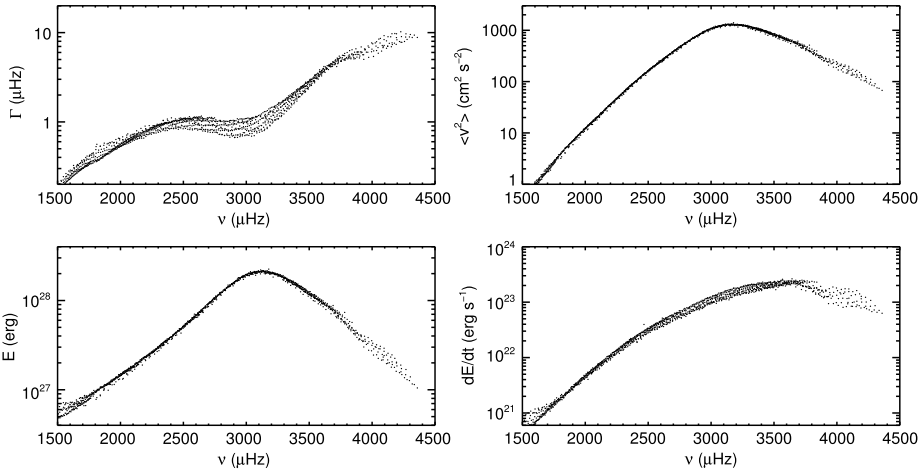

Figure 10 Same as Figure 9, but normalized for mode inertia with Equation 11. Mode energy E is unchanged.

the same behavior with frequency. The ridge structure is not apparent in the mode energies (lower left panel). The difference between mode energy E and the other three quantities is the inclusion of mode inertia, see Equations 6, 7, 9, and 10.

A normalized mode inertia can be calculated by computing the ratio of the mode inertia I_{nl} to the inertia of radial modes $\overline{I_{n0}}$ interpolated to the frequency of the mode ν_{nl} (Christensen-Dalsgaard *et al.*, 1996; Aerts, Christensen-Dalsgaard, and Kurtz, 2010):

$$Q_{nl} = \frac{I_{nl}}{\overline{I_{n0}}(\nu_{nl})}. \tag{11}$$

The result of multiplying mode widths, mean squared velocities, and energy supply rates with Q_{nl} is shown in Figure 10. The overall frequency dependence of the quantities is unchanged. However, ridges of different radial orders are now largely collapsed into one. This can best be observed for $\langle v_{nl}^2 \rangle$ (top right panel), which is only composed of one thin line of data points without any residual ridge structure. The steep gradient in mode inertia at low frequencies is not perfectly represented by scaling Q_{nl} with $\overline{I_{n0}}$. Some of the residual scatter in mode widths, energies, and energy supply rate at low mode frequencies is due to this. Different scalings, *e.g.*, with the interpolated inertia of $l = 50$ modes, give somewhat different results (Komm, Howe, and Hill, 2000b). However, the scatter in the scaled quantities is never completely removed. The remaining dependence observed in mode widths across all frequencies may hold information on a degree dependence of the involved damping mechanisms.

To be able to appreciate the temporal change of the four quantities (mode width, mean squared velocity, mode energy, and mode energy supply rate), the parameters of many modes have to be averaged. As the quantities cover two to three orders of magnitude for the investigated set of modes, the frequency range of averaging has to be restricted. Otherwise, values that differ by orders of magnitude would contribute to the average. In Table 2, the frequency ranges of the modes that were taken for the averaging of the four quantities and the number of modes within these frequency ranges are given. The frequency ranges were chosen to select as many modes as possible with similar parameter values (within about a factor of two).

Table 2 Frequency ranges for averaging of physical quantities, number of modes in this frequency range, and correlation coefficients with the $F_{10.7}$ index.

	Γ	$\langle v^2 \rangle$	E	$\mathrm{d}E/\mathrm{d}t$
Frequency range [μHz]	2400 – 3000	2900 – 3300	2900 – 3300	3000 – 3600
Number of modes	358	237	237	385
Correlation ρ	0.69	−0.88	−0.88	−0.01
p value	$< 10^{-10}$	$< 10^{-10}$	$< 10^{-10}$	0.88

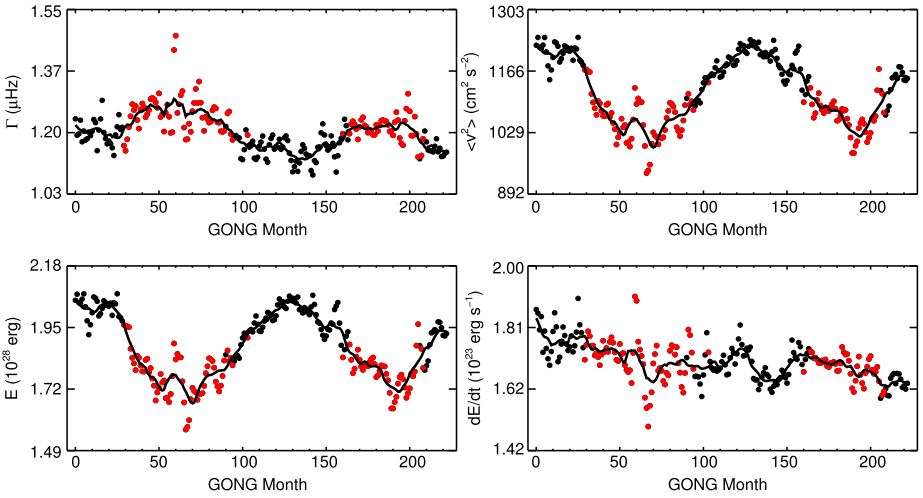

Figure 11 Mode widths Γ, mean squared velocity $\langle v^2 \rangle$, mode energies E, and energy supply rates $\mathrm{d}E/\mathrm{d}t$ as functions of time. Averaged over all modes in the frequency ranges given in Table 2.

The result of this averaging is presented in Figure 11 as a function of time. The red data points indicate times of higher than median level of activity, and the solid black lines are the data smoothed with a one-year boxcar. The last two rows of Table 2 give the rank correlation of independent data points between the four quantities and the $F_{10.7}$ index as well as the two-sided significance value. As before, the mode widths are correlated with the level of magnetic activity with $\rho = 0.69$. The temporal variations in mean squared velocity and mode energy are both highly anticorrelated with the level of solar activity with a value of $\rho = -0.88$. The energy supply rate is not correlated with solar activity for the set of modes investigated here as $\rho = -0.01$ and $p = 0.88$.

5. Summary and Discussion

This study is the first to investigate the activity-related p-mode parameter changes of resolved data covering a complete solar magnetic cycle. We analyzed mode parameter data from the ground-based GONG network. Systematic effects due to the spatial masking of the GONG full-disk solar images, the imperfect temporal sampling, and a yearly modulation due to changes in the apparent radius of the Sun were corrected for. Measurements of mode widths and mode amplitudes are generally less robust than measurements of mode

frequencies. Thus, averages over azimuthal orders as well as modes of different ranges of frequencies and harmonic degrees have to be performed in order to reach meaningful results for the temporal variation of these mode parameters.

Little attention has been given to mode widths and amplitudes (for resolved solar data; Komm, Howe, and Hill, 2000b; Korzennik *et al.*, 2013; Korzennik, 2017 are the most notable exceptions), let alone their temporal variation over the solar cycle. The reason for this is that even without incorporating solar cycle variations, damping widths and amplitudes cannot be accurately modeled with the existing theory of convection and mode excitation (see, *e.g.*, Houdek *et al.*, 1999; Houdek and Dupret, 2015; Basu, 2016). Thanks to the long, uninterrupted GONG time series that is now available, we were now able to investigate the variation of the mode widths and amplitudes as functions of the level of solar activity for different subsets of mode frequencies and harmonic degrees. When the last studies similar to the present one were published, about three years' (Komm, Howe, and Hill, 2000a) and four years' (Komm, Howe, and Hill, 2000b) worth of GONG data had been recorded.

For the mode widths, which were averaged over 1275 modes, we found a variation of $11.5 \pm 0.2\%$ between the minimum and maximum level of activity in the investigated time period. Mode amplitudes varied by $17.3 \pm 0.2\%$ over the same time (averaged over 1272 modes). Overall, the results from previous analyses of the variation of mode widths and amplitudes with the level of solar activity by, *e.g.*, Komm, Howe, and Hill (2000a, 2000b), and Broomhall, Pugh, and Nakariakov (2015) could be confirmed. However, we find a larger variation of mode widths and amplitudes than was expected by Komm, Howe, and Hill (2000a). By extrapolating the fractional change per Gauss of widths and amplitudes to the full minimum-to-maximum change of activity over a solar cycle, they expected widths to vary by 7% and amplitudes to vary by 16% averaged over all modes. Thus, the changes of mode widths we report here are about two-thirds larger than expected by Komm, Howe, and Hill (2000a), while the changes of mode amplitudes agree to within a few percent. The smaller estimated variation of mode widths by Komm, Howe, and Hill (2000a) was most likely due to the shorter time series and differences in which modes they were included.

Like Komm, Howe, and Hill (2000a), we also investigated the change of mode widths and amplitudes for subsets of mode frequencies and harmonic degrees. While they averaged over 100 μHz or five harmonic degrees (their Figures 10 and 11), we did this for larger ranges in frequency and harmonic degree, see Figures 6 – 7 and Tables 3 – 4. We can confirm their findings that the change of mode widths and amplitudes with activity is largest for modes around the frequency of maximum amplitude. We also can confirm that the change is more strongly dependent on mode frequency than it is on harmonic degree: for example, the amplitude of the fractional variation of mode amplitudes for modes with $61 \leq l \leq 100$ is 12.9%, 27.4%, and 19.6% for the low-, mid-, and high-frequency ranges, respectively. Keeping the frequency range the same, the fractional variation of mode amplitudes for modes with $2400 \leq \nu \leq 3300$ is 24.8%, 23.7%, 27.4%, and 18.4% for the four ranges of harmonic degrees in ascending order.

The amplitude of the shifts of mode frequencies with the level of solar activity is known to increase with mode frequency (Jiménez-Reyes *et al.*, 1998; Salabert, García, and Turck-Chièze, 2015). In contrast, this behavior is observed neither for mode widths nor for mode amplitudes. For these two parameters, the largest variation over the solar cycle is observed around the frequency of maximum amplitude $\nu_{\max}$, see Tables 3 and 4, which has been measured by Komm, Howe, and Hill (2000b), see their Table 3. This frequency-dependent variation is in agreement with the theoretical calculations by Houdek *et al.* (2001), who

found that mode damping widths for frequencies between 2500 – 3000 μHz increase with decreasing characteristic size of granulation, *i.e.*, with higher levels of magnetic activity.

Thus, the mechanisms through which the frequencies are changed by the presence of the magnetic field associated with the solar cycle differ from those physical mechanisms that perturb the mode damping widths and amplitudes. Mode widths and amplitudes are determined by the excitation and damping of the acoustic oscillations in very shallow layers, where convection is most vigorous (Balmforth, 1992; Rimmele *et al.*, 1995; Houdek and Dupret, 2015). Hence, this is where the changing magnetic field over the solar cycle affects mode widths and amplitudes most strongly. In contrast to this, mode frequencies can be perturbed by magnetic fields that are located far more deeply in the Sun (see, *e.g.*, Gough and Thompson, 1990). An analysis of the timing of the changes in mode frequencies, amplitudes, and widths may yield information on the evolution and possibly the gradual ascent of magnetic field concentrations through the outer part of the convection zone.

The mode amplitudes as a function of mode frequency were fit with an asymmetric Voigt profile. From this, we found a frequency of maximum amplitude at $\nu_{\max} = 3079.76 \pm 0.17$ μHz. The frequency of maximum amplitude $\nu_{\max}$ is of great interest to asteroseismic studies because it can be used in scaling relations for stellar mass and radius. The value found here compares well to those found in the literature (see the remarks in Section 3.3). Mode amplitudes are a function of radial order and frequency, as can be seen in the top panel of Figure 8. The spread in the distribution of the mode amplitudes as a function of mode frequency could not be removed by multiplication with mode inertia as for, *e.g.*, mean squared velocity of the modes. This indicates that the excitation of modes is intrinsically not only a function of mode frequency. We find that amplitudes of modes of similar harmonic degree follow the asymmetric Voigt profile very well (bottom panel of Figure 8) and that the fit parameters vary with harmonic degrees of the modes, see the discussion in Appendix C.

The physical quantities of mean squared velocity, mode energy, and energy supply rate were calculated from the mode widths and amplitudes. Ridges of the same radial order are evident in the mode widths, mean squared velocities, and the energy supply rates (Figure 9). This was removed by scaling them with their mode inertia Q_{nl} (Figure 10), indicating that Q_{nl} is the correct scaling for mode widths, mean squared velocities, and energy supply rates (Komm, Howe, and Hill, 2000b). The maximum of the velocity of the modes is approximately 37 $\mathrm{cm\,s^{-1}}$. This value is somewhat higher than the value of ≈ 27 $\mathrm{cm\,s^{-1}}$ found by Chaplin *et al.* (1998) for radial modes from BiSON data. As modes of very low harmonic degree (below $l = 10$) are not included in this investigation, it may well be that the velocity of these modes would be closer to the value of Chaplin *et al.* (1998) than that of modes for higher degree. This is supported by the fact that, on closer inspection, modes of lower harmonic degree are concentrated at the lower edge of the distribution shown in the top right panel of Figure 9.

To obtain the temporal variation of these quantities (*i.e.*, mean squared velocity, energy, and energy supply rate; in physical units, not normalized to their temporal mean), an average over modes within a frequency range specific to each quantity (see Table 2) was calculated for the inertia-corrected parameter values.

The average of the mode widths was found to vary between a maximum width of 1.36 ± 0.01 μHz at the maximum of Solar Cycle 23 and a minimum of 1.19 ± 0.01 μHz during the activity minimum between Cycles 23 and 24. The mean squared velocity varied between extrema of 1065 ± 2 $\mathrm{cm^2\,s^{-2}}$ and 1249 ± 4 $\mathrm{cm^2\,s^{-2}}$. The mean mode energy exhibits variation between $1.64 \pm 0.01 \times 10^{28}$ erg and $2.06 \pm 0.01 \times 10^{28}$ erg. This highlights that detectability of solar-like oscillation is reduced in stars with high levels of magnetic activity, as has been investigated and shown by Chaplin *et al.* (2011). These fractional changes

are considerably different for modes of different frequencies, as can be seen from Figures 6 and 7. Qualitatively, our results agree with those of, *e.g.*, Komm, Howe, and Hill (2000b), Jiménez-Reyes *et al.* (2003), and Salabert and Jiménez-Reyes (2006). The differences in the included mode degrees and frequencies and in the length of the data make it somewhat difficult to quantitatively compare the measured fractional parameter changes.

The variation in mean energy supply rate, shown in the lower right panel of Figure 11, is not correlated with the level of solar activity for the investigated set of modes. This confirms the results of, *e.g.*, Chaplin *et al.* (2000), Jiménez-Reyes *et al.* (2003), and Broomhall, Pugh, and Nakariakov (2015), who found that the energy supply rate to solar p modes of low harmonic degrees does not change with the level of activity. Overall, there is a decrease in supply rates over the observed time period of about 8%. However, this decrease happened entirely before GONG month 60, hence, before the upgrade of the GONG network. Since then, it has remained at a rather constant level. A dedicated study of energy supply rates, focusing on mode sets from different frequency ranges and harmonic degree ranges, as we did in Sections 3.1 and 3.2 for mode widths and amplitudes, will give further insight into whether the energy supply rates are truly constant over the solar cycle.

Acknowledgements This work utilizes data obtained by the *Global Oscillation Network Group* (GONG) Program, managed by the National Solar Observatory, which is operated by AURA, Inc. under a cooperative agreement with the National Science Foundation. The data were acquired by instruments operated by the Big Bear Solar Observatory, High Altitude Observatory, Learmonth Solar Observatory, Udaipur Solar Observatory, Instituto de Astrofísica de Canarias, and Cerro Tololo Interamerican Observatory. RK & AMB acknowledge the support of the STFC consolidated grant ST/P000320/1. The research leading to these results has received funding from the European Research Council (ERC) under the European Union's Seventh Framework Program (FP/2007-2013)/ERC Grant Agreement n. 307117. This work was supported by the SOLARNET project funded by the European Commission's FP7 Capacities Programme under the Grant Agreement 312495.

Disclosure of Potential Conflicts of Interest The authors declare that they have no conflicts of interest.

Appendix A: Correction for Jumps in Mode Amplitudes

The cameras of the GONG network were upgraded from 256 × 256 rectangular pixels to 1024 × 1024 square pixels around GONG month 60[3] (Harvey, Tucker, and Britanik, 1998). Care was taken to minimize the effect of the transition between the two sets of instrumentation on the measured mode parameters by updating the data reduction and peak-finding pipeline (Toner *et al.*, 2003; Hughes *et al.*, 2016). However, a clear jump in the mode amplitudes is visible at the time of the network upgrade. This can be seen in Figure 12, which shows the fractional variation of mean uncorrected mode amplitudes as a function of time for modes of different ranges of harmonic degree and mode frequency. As a complete reprocessing of the original data is not feasible, we removed this jump for each mode by matching the parameters on either side of the jump using a correction factor C, which is given in Equation 12. This factor is dependent on the frequency and the harmonic degree of the mode.

[3]For a table with the exact dates of the GONG months, see gong.nso.edu/data/DMAC_documentation/gongmonths.html.

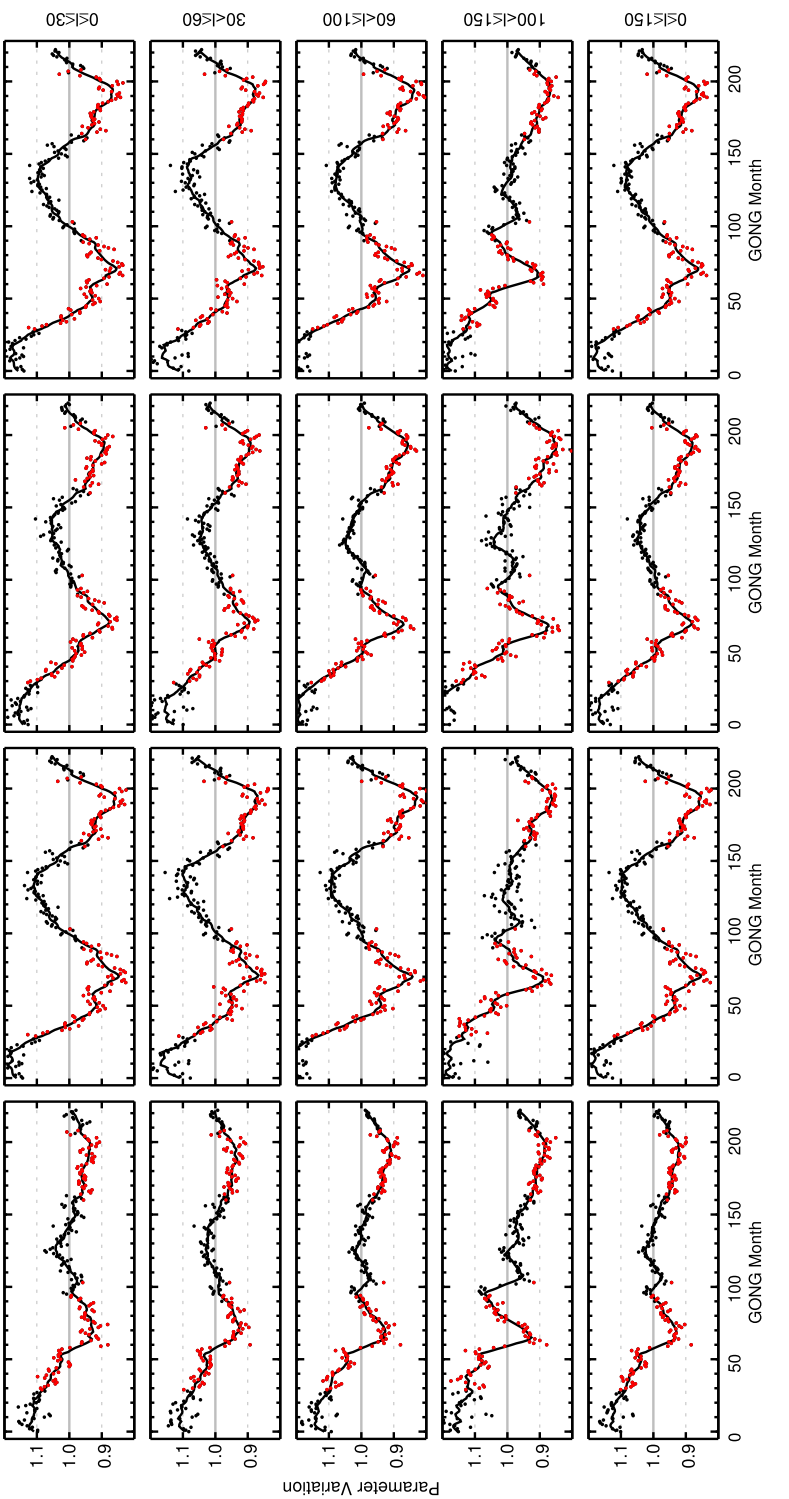

Figure 12 Temporal variation of mode amplitudes that are not corrected for jumps in the data. Different ranges of harmonic degrees (*rows*, harmonic degree indicated to the right of the fourth column) and mode frequencies (*columns*, frequency range indicated above the first row) are shown. Amplitudes are normalized to the mean for each mode and then averaged over all modes in the respective range of frequency and degree. Months with higher than median 10.7 cm solar radio flux are highlighted by *red data points*. The one-year average is shown by the *black solid curve*. Levels of 1.1 and 0.9 of the mean are indicated by *gray dashed lines*.

There is another jump at month 100, which only affects mode amplitudes and parameters that involve mode amplitudes (see Figure 12). We were not able to relate this jump to a change in the instrumentation or the processing pipeline. Therefore, we also patched this jump by multiplying the mode amplitudes after month 100 with a correction factor (Equation 12). As can be seen in Figure 12, the magnitude of the jumps are dependent on mode frequency (at month 60) and on harmonic degree (both at month 60 and at month 100). We included a linear term in mode frequency and a term linear in harmonic degree to the correction factor given in Equation 12. After applying the correction for the jump at month 60, there is strong temporal variation in mode amplitudes around this time (± 3 months). This variation does not follow a simple step-like function and is not further corrected for. Its cause is probably the incremental switch to the upgraded cameras across the network over several months.

The correction factors that the mode amplitudes were multiplied by in the indicated time frame are

$$
\begin{aligned}
C &= 1 - \frac{0.03 \cdot l}{150} - \frac{0.06 \cdot \nu}{4500\,\mu\text{Hz}} - 0.06 && \text{(months 1 – 58)},\\
C &= 1 - \frac{0.02 \cdot l}{150} - \frac{0.04 \cdot \nu}{4500\,\mu\text{Hz}} - 0.04 && \text{(month 59)},\\
C &= 1 - \frac{0.01 \cdot l}{150} - \frac{0.02 \cdot \nu}{4500\,\mu\text{Hz}} - 0.02 && \text{(month 60)},\\
C &= 1 && \text{(months 61 – 98)},\\
C &= 1 + \frac{0.0733 \cdot l}{150} && \text{(month 100)},\\
C &= 1 + \frac{0.1466 \cdot l}{150} && \text{(month 101)},\\
C &= 1 + \frac{0.22 \cdot l}{150} && \text{(months 102 – 223)},
\end{aligned}
\tag{12}
$$

where l is the harmonic degree of the mode and ν is the frequency of the mode. The corrections around month 60 and month 100 were found empirically. Technicians and software experts of GONG were not able to find a documented change of the instrumentation or the processing pipeline that could affect the data around month 100 in this way. As the hardware was definitely not changed at this time, the jump is probably due to an undocumented and/or unwanted change in the data processing, possibly due to an update of a software library. As the magnitude of the jump is clearly dependent on harmonic degree, see Figure 12, one possibility is that the spherical harmonic functions that were used to calculate the spherical harmonic time series changed in an unnoticed way.

No correction factor was applied to the mode widths. There is no clear jump visible around months 60 or 100 for mode widths. As can be seen in the fourth panel of the first column of Figure 6, which shows the fractional change of widths of modes with frequencies 1500 – 2400 μHz and harmonic degrees 100 – 150, around month 45 there is a rapid change in mode widths. As this is only seen for mode widths in this small sub-set of modes, we chose not to apply a correction in this case.

Appendix B: Results for Normalized Mode Parameter Variation

See Tables 3 and 4.

Table 3 Results from the normalized and averaged variation of mode width for different parameter ranges shown in Figure 6. *Columns 1–4:* Parameter ranges of the individual panels. *Column 5:* Number of modes included. *Columns 6–7:* Extrema of the one-year smoothed parameter variation *Column 8:* Typical error on the individual unsmoothed data point. *Columns 9–10:* Spearman's correlation coefficient between independent data points of the unsmoothed parameter variation and the $F_{10.7}$ index and the associated p value.

Frequency range [μHz]		Harmonic degrees		Number of modes	Normalized width [%]		Mean error [%]	ρ	p
ν_{min}	ν_{max}	l_{min}	l_{max}		min	max			
1500	2400	0	30	119	96.7 ± 0.2	105.1 ± 0.2	0.6	0.38	$6.7 \cdot 10^{-4}$
2400	3300	0	30	167	93.0 ± 0.2	107.8 ± 0.2	0.5	0.84	$< 10^{-10}$
3300	4500	0	30	101	97.4 ± 0.2	103.5 ± 0.2	0.5	0.70	$< 10^{-10}$
1500	4500	0	30	387	95.7 ± 0.1	105.1 ± 0.1	0.3	0.80	$< 10^{-10}$
1500	2400	31	60	122	95.0 ± 0.1	106.7 ± 0.2	0.4	0.31	$6.3 \cdot 10^{-3}$
2400	3300	31	60	152	86.7 ± 0.1	113.3 ± 0.2	0.4	0.50	$5.2 \cdot 10^{-6}$
3300	4500	31	60	123	95.8 ± 0.2	104.0 ± 0.2	0.4	0.50	$5 \cdot 10^{-6}$
1500	4500	31	60	397	92.2 ± 0.1	108.4 ± 0.1	0.3	0.46	$3.6 \cdot 10^{-5}$
1500	2400	61	100	130	96.6 ± 0.1	104.7 ± 0.1	0.3	0.32	$4.7 \cdot 10^{-3}$
2400	3300	61	100	136	90.7 ± 0.1	109.0 ± 0.1	0.3	0.77	$< 10^{-10}$
3300	4500	61	100	88	94.9 ± 0.1	104.9 ± 0.2	0.4	0.80	$< 10^{-10}$
1500	4500	61	100	354	93.9 ± 0.1	106.2 ± 0.1	0.2	0.69	$< 10^{-10}$
1500	2400	101	150	124	97.6 ± 0.1	103.1 ± 0.1	0.3	0.39	$5.3 \cdot 10^{-4}$
2400	3300	101	150	7	95.6 ± 0.5	104.2 ± 0.5	1.5	0.49	$6.4 \cdot 10^{-6}$
3300	4500	101	150	6	95.4 ± 0.3	105.4 ± 0.6	1.3	0.78	$< 10^{-10}$
1500	4500	101	150	137	97.4 ± 0.1	103.2 ± 0.1	0.3	0.45	$4.3 \cdot 10^{-5}$
1500	2400	0	150	495	96.7 ± 0.1	104.3 ± 0.1	0.2	0.36	$1.7 \cdot 10^{-3}$
2400	3300	0	150	462	90.3 ± 0.1	109.2 ± 0.1	0.3	0.68	$< 10^{-10}$
3300	4500	0	150	318	96.2 ± 0.1	103.6 ± 0.1	0.3	0.74	$< 10^{-10}$
1500	4500	0	150	1275	94.4 ± 0.1	105.9 ± 0.1	0.2	0.62	$2 \cdot 10^{-9}$

Table 4 Results from the normalized and averaged variation of mode amplitudes for different parameter ranges shown in Figure 7. *Columns 1–4:* Parameter ranges of the individual panels. *Column 5:* Number of modes included. *Columns 6–7:* Extrema of the one-year smoothed parameter variation. *Column 8:* Typical error on the individual unsmoothed data point. *Columns 9–10:* Spearman's correlation coefficient between independent data points of the unsmoothed parameter variation and the $F_{10.7}$ index and the associated p value.

Frequency range [μHz]		Harmonic degrees		Number of modes	Normalized amplitude [%]		Mean error [%]	ρ	p
$\nu_{\min}$	$\nu_{\max}$	$l_{\min}$	$l_{\max}$		min	max			
1500	2400	0	30	119	94.6 ± 0.3	106.2 ± 0.4	1.2	−0.82	$< 10^{-10}$
2400	3300	0	30	164	87.7 ± 0.2	112.5 ± 0.3	0.9	−0.94	$< 10^{-10}$
3300	4500	0	30	101	93.5 ± 0.2	105.1 ± 0.3	0.8	−0.88	$< 10^{-10}$
1500	4500	0	30	384	91.4 ± 0.2	108.5 ± 0.2	0.6	−0.92	$< 10^{-10}$
1500	2400	31	60	122	94.4 ± 0.2	106.9 ± 0.2	0.7	−0.78	$< 10^{-10}$
2400	3300	31	60	152	88.8 ± 0.1	112.5 ± 0.2	0.5	−0.88	$< 10^{-10}$
3300	4500	31	60	123	93.2 ± 0.1	107.1 ± 0.2	0.4	−0.88	$< 10^{-10}$
1500	4500	31	60	397	91.9 ± 0.1	109.0 ± 0.1	0.3	−0.87	$< 10^{-10}$
1500	2400	61	100	130	94.6 ± 0.1	107.5 ± 0.2	0.5	−0.76	$< 10^{-10}$
2400	3300	61	100	136	86.7 ± 0.1	114.1 ± 0.2	0.5	−0.91	$< 10^{-10}$
3300	4500	61	100	88	90.3 ± 0.1	109.9 ± 0.2	0.5	−0.89	$< 10^{-10}$
1500	4500	61	100	354	90.6 ± 0.1	110.6 ± 0.1	0.3	−0.90	$< 10^{-10}$
1500	2400	101	150	124	94.0 ± 0.1	107.4 ± 0.2	0.5	−0.66	$< 10^{-9}$
2400	3300	101	150	7	90.5 ± 0.4	108.9 ± 0.7	1.8	−0.82	$< 10^{-10}$
3300	4500	101	150	6	89.1 ± 0.4	112.2 ± 0.7	1.7	−0.87	$< 10^{-10}$
1500	4500	101	150	137	93.8 ± 0.1	107.7 ± 0.2	0.5	−0.70	$< 10^{-10}$
1500	2400	0	150	495	95.0 ± 0.1	106.9 ± 0.1	0.4	−0.81	$< 10^{-10}$
2400	3300	0	150	459	87.8 ± 0.1	112.9 ± 0.1	0.4	−0.92	$< 10^{-10}$
3300	4500	0	150	318	92.4 ± 0.1	107.3 ± 0.1	0.3	−0.90	$< 10^{-10}$
1500	4500	0	150	1272	91.8 ± 0.1	109.1 ± 0.1	0.2	−0.91	$< 10^{-10}$

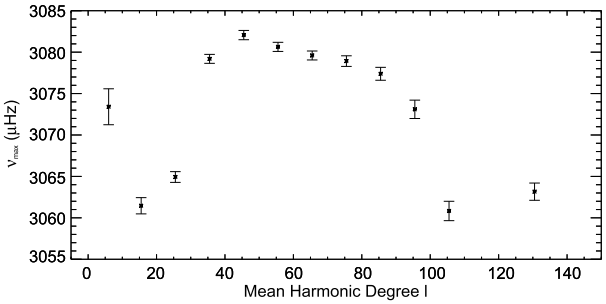

Figure 13 Frequency of maximum amplitude $\nu_{\max}$ for different ranges of harmonic degrees.

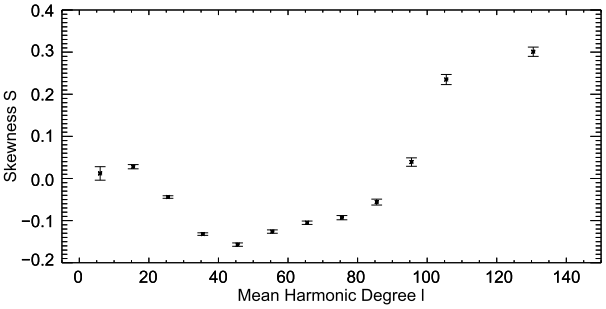

Figure 14 Same as Figure 13, but for the skewness S.

Appendix C: Results of fits to mode amplitudes for different ranges of harmonic degrees

To investigate the degree dependence of the mode amplitudes, we separated the modes into groups of typically ten harmonic degrees, see the first column of Table 5. We excluded modes with $l = 0, 1$ because their amplitudes are significantly different from those of modes with $2 \leq l \leq 10$ (see Figure 8 of Howe *et al.*, 2003 for mean mode heights of low-degree modes from GONG). In order to achieve a good fit of the mode amplitudes for modes with $l > 110$, we grouped together the range covering degrees $111 \leq l \leq 150$. We included all modes that were present in at least 50% of the GONG months. Lowering the presence rate from 100% was necessary because there were not enough modes present in certain frequency ranges and the fits did not converge properly. We describe the Voigt profile and the fit results of the complete set of modes $l = 2-150$ in Section 3.3. There, we also present a fit to the amplitudes of the group $31 \leq l \leq 40$ (bottom panel of Figure 8).

Figures 13–16 show the fit parameter frequency of maximum amplitude $\nu_{\max}$, skewness S, width of the asymmetric Voigt Σ, and amplitude parameter a as functions of the mean harmonic degree of the ranges listed in the first column of Table 5.

In Figure 13 it can be seen that $\nu_{\max}$ first decreases from the group of lowest degree modes to second and third group before it increases. It is then more or less constant for modes with $31 \leq l \leq 90$ and decreases again for higher degree modes. The skewness S, shown in Figure 14, is close to 0 for modes $l < 21$, negative for modes with $21 \leq l \leq 90$, and turns positive for modes with $l > 90$. The frequency of maximum amplitude $\nu_{\max}$ and the skewness S are strongly anticorrelated with a rank correlation of $\rho = -0.91$ and a p value $< 3 \cdot 10^{-5}$.

The width of the Voigt profile changes by only about 3% for modes with $2 \leq l \leq 110$. The much larger Σ of the group with $111 \leq l \leq 150$ is probably due to the wider range of

Table 5 Fit parameters of the frequency distribution of mode amplitudes for different ranges of harmonic degrees.

Range of degrees l	$\nu_{\max}$ [μHz]	σ [μHz]	γ [μHz]	Σ [μHz]	$a/10^4$ [$m^2\,s^{-2}\,Hz^{-1}$]	b [$m^2\,s^{-2}\,Hz^{-1}$]	S	Number of modes	χ^2_{red}
2 – 10	3073.41 ± 2.17	166.5 ± 2.9	161.0 ± 2.6	591.8 ± 7.1	2800 ± 14	-640 ± 19	0.012 ± 0.016	132	9.3
11 – 20	3061.46 ± 0.98	169.2 ± 1.4	153.5 ± 1.1	587.5 ± 3.3	3140 ± 9	-611 ± 7	0.028 ± 0.005	175	6.4
21 – 30	3064.93 ± 0.65	168.5 ± 0.9	156.1 ± 0.7	589.3 ± 2.2	3397 ± 6	-655 ± 5	-0.044 ± 0.003	172	10.4
31 – 40	3079.19 ± 0.54	177.0 ± 0.7	152.6 ± 0.5	603.5 ± 1.6	3424 ± 4	-630 ± 3	-0.132 ± 0.003	157	10.8
41 – 50	3082.06 ± 0.56	174.9 ± 0.7	153.3 ± 0.5	599.8 ± 1.6	3470 ± 4	-638 ± 3	-0.157 ± 0.004	134	9.9
51 – 60	3080.64 ± 0.55	175.4 ± 0.7	153.0 ± 0.5	600.5 ± 1.6	3461 ± 4	-619 ± 3	-0.126 ± 0.004	118	13.1
61 – 70	3079.60 ± 0.54	174.4 ± 0.7	154.1 ± 0.5	599.8 ± 1.6	3418 ± 3	-594 ± 3	-0.105 ± 0.004	113	9.7
71 – 80	3078.92 ± 0.64	165.6 ± 0.8	164.1 ± 0.7	594.3 ± 2.0	3395 ± 4	-660 ± 4	-0.093 ± 0.005	99	9.0
81 – 90	3077.39 ± 0.78	160.9 ± 1.1	173.6 ± 0.9	597.5 ± 2.6	3360 ± 5	-706 ± 5	-0.056 ± 0.007	89	8.8
91 – 100	3073.10 ± 1.11	150.3 ± 1.7	189.0 ± 1.5	597.3 ± 4.0	3336 ± 7	-734 ± 8	0.039 ± 0.010	79	13.2
101 – 110	3060.83 ± 1.17	127.4 ± 3.0	217.0 ± 2.7	593.8 ± 6.6	3429 ± 12	-780 ± 10	0.235 ± 0.012	80	11.2
111 – 150	3063.16 ± 1.04	142.6 ± 2.3	220.6 ± 2.3	629.4 ± 5.4	3369 ± 10	-804 ± 9	0.301 ± 0.011	195	19.1

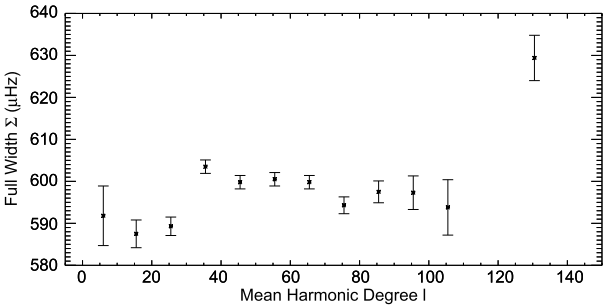

Figure 15 Same as Figure 13, but for the width of the Voigt profile Σ.

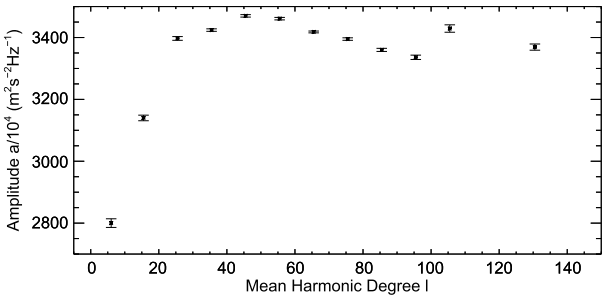

Figure 16 Same as Figure 13, but for the amplitude parameter a.

modes included in this group (see also Section 3.3). The amplitude parameter a (Figure 16) increases for the first three groups of harmonic degrees from 2800 ± 14 m^2 s^{-2} Hz^{-1} for $2 \leq l \leq 10$ to 3424 ± 4 m^2 s^{-2} Hz^{-1} for $31 \leq l \leq 40$. Compared to this large increase, the amplitude parameter changes very little for the groups of modes of higher degrees.

References

Aerts, C., Christensen-Dalsgaard, J., Kurtz, D.W.: 2010, *Asteroseismology*, Springer, Dordrecht, 470. DOI. ADS.

Anderson, E.R., Duvall, J., Thomas, L., Jefferies, S.M.: 1990, Modeling of solar oscillation power spectra. *Astrophys. J.* **364**, 699. DOI. ADS.

Balmforth, N.J.: 1992, Solar pulsational stability – III. Acoustical excitation by turbulent convection. *Mon. Not. Roy. Astron. Soc.* **255**, 639. DOI. ADS.

Basu, S.: 2016, Global seismology of the Sun. *Living Rev. Solar Phys.* **13**, 2. DOI. ADS.

Broomhall, A.-M.: 2017, A helioseismic perspective on the depth of the minimum between Solar Cycles 23 and 24. *Solar Phys.* **292**, 67. DOI. ADS.

Broomhall, A.-M., Nakariakov, V.M.: 2015, A comparison between global proxies of the Sun's magnetic activity cycle: Inferences from helioseismology. *Solar Phys.* **290**, 3095. DOI. ADS.

Broomhall, A.-M., Pugh, C.E., Nakariakov, V.M.: 2015, Solar cycle variations in the powers and damping rates of low-degree solar acoustic oscillations. *Adv. Space Res.* **56**, 2706. DOI. ADS.

Broomhall, A.-M., Chaplin, W.J., Davies, G.R., Elsworth, Y., Fletcher, S.T., Hale, S.J., Miller, B., New, R.: 2009, Definitive Sun-as-a-star p-mode frequencies: 23 years of BiSON observations. *Mon. Not. Roy. Astron. Soc. Lett.* **396**, L100. DOI. ADS.

Burtseva, O., Hill, F., Kholikov, S., Chou, D.-Y.: 2009, Lifetimes of high-degree p modes in the quiet and active Sun. *Solar Phys.* **258**(1), 1. DOI. ADS.

Chaplin, W.J., Elsworth, Y., Isaak, G.R., Lines, R., McLeod, C.P., Miller, B.A., New, R.: 1998, Solar p-mode excitation: Further insight from recent low-l BiSON helioseismological data. *Mon. Not. Roy. Astron. Soc.* **298**, L7. DOI. ADS.

Chaplin, W.J., Elsworth, Y., Isaak, G.R., Miller, B.A., New, R.: 2000, Variations in the excitation and damping of low-ℓ solar p modes over the solar activity cycle. *Mon. Not. Roy. Astron. Soc.* **313**, 32. DOI. ADS.

Chaplin, W.J., Appourchaux, T., Elsworth, Y., Isaak, G.R., New, R.: 2001, The phenomenology of solar-cycle-induced acoustic eigenfrequency variations: A comparative and complementary analysis of GONG, BiSON and VIRGO/LOI data. *Mon. Not. Roy. Astron. Soc.* **324**(4), 910. DOI. ADS.

Chaplin, W.J., Bedding, T.R., Bonanno, A., Broomhall, A.-M., García, R.A., Hekker, S., Huber, D., Verner, G.A., Basu, S., Elsworth, Y., Houdek, G., Mathur, S., Mosser, B., New, R., Stevens, I.R., Appourchaux, T., Karoff, C., Metcalfe, T.S., Molenda-Żakowicz, J., Monteiro, M.J.P.F.G., Thompson, M.J., Christensen-Dalsgaard, J., Gilliland, R.L., Kawaler, S.D., Kjeldsen, H., Ballot, J., Benomar, O., Corsaro, E., Campante, T.L., Gaulme, P., Hale, S.J., Handberg, R., Jarvis, E., Regulo, C., Roxburgh, I.W., Salabert, D., Stello, D., Mullally, F., Li, J., Wohler, W.: 2011, Evidence for the impact of stellar activity on the detectability of solar-like oscillations observed by Kepler. *Astrophys. J. Lett.* **732**, L5. DOI. ADS.

Christensen-Dalsgaard, J., Berthomieu, G.: 1991, Theory of solar oscillations. In: Cox, A.N., Livingston, W.C., Matthews, M. (eds.) *Solar Interior and Atmosphere*, University of Arizona Press, Tucson, 401. ADS.

Christensen-Dalsgaard, J., Däppen, W., Ajukov, S.V., Anderson, E.R., Antia, H.M., Basu, S., *et al.*: 1996, The current state of solar modeling. *Science* **272**, 1286. DOI. ADS.

Elsworth, Y., Howe, R., Isaak, G.R., McLeod, C.P., New, R.: 1990, Variation of low-order acoustic solar oscillations over the solar cycle. *Nature* **345**(6273), 322. DOI. ADS.

Elsworth, Y., Howe, R., Isaak, G.R., McLeod, C.P., Miller, B.A., New, R., Speake, C.C., Wheeler, S.J.: 1993, The variation in the strength of low-ℓ solar p-modes: 1981 – 92. *Mon. Not. Roy. Astron. Soc.* **265**(4), 888. DOI. ADS.

Goldreich, P., Murray, N., Kumar, P.: 1994, Excitation of solar p-modes. *Astrophys. J.* **424**, 466. DOI. ADS.

Gough, D.O., Thompson, M.J.: 1990, The effect of rotation and a buried magnetic field on stellar oscillations. *Mon. Not. Roy. Astron. Soc.* **242**, 25. DOI. ADS

Harvey, J., Tucker, R., Britanik, L.: 1998, High resolution upgrade of the GONG instruments. In: Korzennik, S. (ed.) *Structure and Dynamics of the Interior of the Sun and Sun-like Stars*, *ESA-SP* **418**, ESA Publications Division, Noordwijk, 209. ADS.

Hill, F., Howe, R.: 1998, Calculating the GONG leakage matrix. In: Korzennik, S.G., Wilson, A. (eds.) *Structure and Dynamics of the Interior of the Sun and Sun-like Stars*, *ESA-SP* **418**, ESA Publications Division, Noordwijk, 225. ADS.

Hill, F., Stark, P.B., Stebbins, R.T., Anderson, E.R., Antia, H.M., Brown, T.M., *et al.*: 1996, The solar acoustic spectrum and eigenmode parameters. *Science* **272**, 1292. DOI. ADS.

Houdek, G., Dupret, M.-A.: 2015, Interaction between convection and pulsation. *Living Rev. Solar Phys.* **12**, 8. DOI. ADS.

Houdek, G., Balmforth, N.J., Christensen-Dalsgaard, J., Gough, D.O.: 1999, Amplitudes of stochastically excited oscillations in main-sequence stars. *Astron. Astrophys.* **351**, 582. ADS.

Houdek, G., Chaplin, W.J., Appourchaux, T., Christensen-Dalsgaard, J., Dappen, W., Elsworth, Y., *et al.*: 2001, Changes in convective properties over the solar cycle: Effect on p-mode damping rates. *Mon. Not. Roy. Astron. Soc.* **327**(2), 483. DOI. ADS.

Howe, R., Chaplin, W.J., Elsworth, Y.P., Hill, F., Komm, R., Isaak, G.R., New, R.: 2003, A comparison of low-degree solar p-mode parameters from BiSON and GONG: Underlying values and temporal variations. *Astrophys. J.* **588**(2), 1204. DOI. ADS.

Howe, R., Haber, D.A., Hindman, B.W., Komm, R., Hill, F., Gonzalez Hernandez, I.: 2008, Helioseismic frequency shifts in active regions. In: Howe, R., Komm, R.W., Balasubramaniam, R.S., Petrie, G.J.D. (eds.) *Subsurface and Atmospheric Influences on Solar Activity*, *ASP Conf. Ser.* **383**, Astron. Soc. Pac., San Francisco, 305. ADS.

Howe, R., Davies, G.R., Chaplin, W.J., Elsworth, Y.P., Hale, S.J.: 2015, Validation of solar-cycle changes in low-degree helioseismic parameters from the Birmingham Solar-Oscillations Network. *Mon. Not. Roy. Astron. Soc.* **454**, 4120. DOI. ADS.

Hughes, A.L.H., Jain, K., Kholikov, S. (NISP Solar Interior Group): 2016, GONG ClassicMerge: Pipeline and product. arXiv. ADS.

Jefferies, S.M., Pomerantz, M.A., Duvall, T.L., Harvey, J.W., Osaki, Y.: 1991, Characteristics of intermediate-degree solar p-mode line widths. *Astrophys. J.* **377**, 330. DOI. ADS.

Jiménez, A., Roca Cortés, T., Jiménez-Reyes, S.J.: 2002, Variation of the low-degree solar acoustic mode parameters over the solar cycle. *Solar Phys.* **209**(2), 247. DOI. ADS.

Jiménez-Reyes, S.J., Régulo, C., Pallé, P.L., Roca Cortes, T.: 1998, Solar activity cycle frequency shifts of low-degree p-modes. *Astron. Astrophys.* **329**, 1119. ADS.

Jiménez-Reyes, S.J., Garcia, R.A., Jimenez, A., Chaplin, W.J.: 2003, Excitation and damping of low-degree solar p-modes during Activity Cycle 23: Analysis of GOLF and VIRGO Sun Photometer Data. *Astrophys. J.* **595**(1), 446. DOI. ADS.

Jiménez-Reyes, S.J., Chaplin, W.J., Elsworth, Y., García, R.A.: 2004, Tracing the "acoustic" Solar Cycle: A direct comparison of BiSON and GOLF Low-l p-mode variations. *Astrophys. J.* **604**(2), 969. DOI. ADS.

Jiménez-Reyes, S.J., Chaplin, W.J., Elsworth, Y., Garcia, R.A., Howe, R., Socas-Navarro, H., Toutain, T.: 2007, On the variation of the peak asymmetry of low-l solar p modes. *Astrophys. J.* **654**, 1135. DOI. ADS.

Kallinger, T., Mosser, B., Hekker, S., Huber, D., Stello, D., Mathur, S., Basu, S., Bedding, T.R., Chaplin, W.J., De Ridder, J., Elsworth, Y.P., Frandsen, S., García, R.A., Gruberbauer, M., Matthews, J.M., Borucki, W.J., Bruntt, H., Christensen-Dalsgaard, J., Gilliland, R.L., Kjeldsen, H., Koch, D.G.: 2010, Asteroseismology of red giants from the first four months of Kepler data: Fundamental stellar parameters. *Astron. Astrophys.* **522**, A1. DOI. ADS.

Kjeldsen, H., Bedding, T.R.: 1995, Amplitudes of stellar oscillations: The implications for asteroseismology. *Astron. Astrophys.* **293**, 87. ADS.

Komm, R.W., Howe, R., Hill, F.: 2000a, Solar-cycle changes in gong p-mode widths and amplitudes 1995 – 1998. *Astrophys. J.* **531**, 1094. DOI. ADS.

Komm, R.W., Howe, R., Hill, F.: 2000b, Width and energy of solar p-modes observed by Global Oscillation Network Group. *Astrophys. J.* **543**, 472. DOI. ADS.

Korzennik, S.G.: 2013, Mode frequencies from GONG, MDI, and HMI data. In: Jain, K., Tripathy, S.C., Hill, F., Leibacher, J.W., Pevtsov, A.A. (eds.) *Fifty Years of Seismology of the Sun and Stars*, *Astron. Soc. Pac. Conf. Ser.* **478**, Astron. Soc. Pac., San Francisco, 137. ADS.

Korzennik, S.G.: 2017, Initial results from fitting p-modes using intensity observations from the Helioseismic and Magnetic Imager. *Solar Phys.* **292**, 138. DOI. ADS.

Korzennik, S.G., Rabello-Soares, M.C., Schou, J., Larson, T.P.: 2013, Accurate characterization of high-degree modes using MDI observations. *Astrophys. J.* **772**, 87. DOI. ADS.

Kumar, P., Franklin, J., Goldreich, P.: 1988, Distribution functions for the time-averaged energies of stochastically excited solar p-modes. *Astrophys. J.* **328**, 879. DOI. ADS.

Leibacher, J.W.: 1999, The Global Oscillation Network Group (GONG) project. *Adv. Space Res.* **24**, 173. DOI. ADS.

Libbrecht, K.G., Woodard, M.F.: 1990, Solar-cycle effects on solar oscillation frequencies. *Nature* **345**(6278), 779. DOI. ADS.

Macris, C.J., Mueller, R., Rosch, J., Roudier, T.: 1984, Variation of the mesh of the granular network along the Solar Cycle. In: Keil, S. (ed.) *Small-Scale Dynamical Processes in Quiet Stellar Atmospheres*, National Solar Observatory, Sunspot, 265. ADS.

Mosser, B., Michel, E., Belkacem, K., Goupil, M.J., Baglin, A., Barban, C., Provost, J., Samadi, R., Auvergne, M., Catala, C.: 2013, Asymptotic and measured large frequency separations. *Astron. Astrophys.* **550**, A126. DOI. ADS.

Muller, R.: 1988, Variability of solar granulation. *Adv. Space Res.* **8**(7), 159. DOI. ADS.

Muller, R., Hanslmeier, A., Saldaña-Muñoz, M.: 2007, Variations of the granulation related to the solar cycle and with respect to its position on the solar disk. *Astron. Astrophys.* **475**(2), 717. DOI. ADS.

Nigam, R., Kosovichev, A.G., Scherrer, P.H., Schou, J.: 1998, Asymmetry in velocity and intensity helioseismic spectra: A solution to a long-standing puzzle. *Astrophys. J. Lett.* **495**, L115. DOI. ADS.

Olivero, J.J., Longbothum, R.L.: 1977, Empirical fits to the Voigt line width: A brief review. *J. Quant. Spectrosc. Radiat. Transf.* **17**, 233. DOI. ADS.

Pallé, P.L., Régulo, C., Roca Cortés, T.: 1990, The spectrum of solar p-modes and the solar activity cycle. In: Osaki, Y., Shibahashi, H. (eds.) *Progress of Seismology of the Sun and Stars*, *Lecture Notes in Physics* **367**, Springer, Berlin, 129. DOI. ADS.

Rhodes, E.J., Reiter, J., Schou, J., Larson, T., Scherrer, P., Brooks, J., McFaddin, P., Miller, B., Rodriguez, J., Yoo, J.: 2010, Temporal changes in the frequencies of the solar p-mode oscillations during solar cycle 23. In: Choudhary, D.P., Strassmeier, K.G. (eds.) *Proc. IAU: The Physics of Sun and Star Spots* **6**, International Astronomical Union, Cambridge, 389. DOI. ADS.

Rimmele, T.R., Goode, P.R., Harold, E., Stebbins, R.T.: 1995, Dark lanes in granulation and the excitation of solar oscillations. *Astrophys. J. Lett.* **444**, L119. DOI. ADS.

Salabert, D., García, R.A., Turck-Chièze, S.: 2015, Seismic sensitivity to sub-surface solar activity from 18 yr of GOLF/SoHO observations. *Astron. Astrophys.* **578**, A137. DOI. ADS.

Salabert, D., Jiménez-Reyes, S.J.: 2006, Damping and excitation variations of the solar acoustic modes using LOWL observations. *Astrophys. J.* **650**(1), 451. DOI. ADS.

Salabert, D., Chaplin, W.J., Elsworth, Y., New, R., Verner, G.A.: 2007, Sun-as-a-star observations: evidence for degree dependence of changes in damping of low-l p modes along the solar cycle. *Astron. Astrophys.* **463**(3), 1181. DOI. ADS.

Tapping, K.F.: 2013, The 10.7 cm solar radio flux (F10.7). *Space Weather* **11**, 394. DOI. ADS.

Toner, C.G., Haber, D., Corbard, T., Bogart, R., Hindman, B.: 2003, An image merge for GONG+. In: Sawaya-Lacoste, H. (ed.) *Proc. SOHO 12/GONG+ 2002. Local and Global Helioseismology: The Present and Future*, *ESA-SP* **517**, ESA Publications Division, Noordwijk, 405. ADS.

Tripathy, S.C., Jain, K., Hill, F.: 2015, Variations in high degree acoustic mode frequencies of the Sun during Solar Cycle 23 and 24. *Astrophys. J.* **812**(1), 20. DOI. ADS.

Whiting, E.E.: 1968, An empirical approximation to the Voigt profile. *J. Quant. Spectrosc. Radiat. Transf.* **8**, 1379. DOI. ADS.

Woodard, M.F., Libbrecht, K.G.: 1991, Is there an acoustic resonance in the solar chromosphere? *Astrophys. J.* **374**(2), L61. DOI. ADS.

Woodard, M.F., Noyes, R.W.: 1985, Change of solar oscillation eigenfrequencies with the solar cycle. *Nature* **318**(6045), 449. DOI. ADS.